Review Article

Nano Research
2022, 15(8): 6862–6887

ISSN 1998-0124 CN 11-5974/O4
https://doi.org/10.1007/s12274-022-4297-3

# Modulation of morphology and electronic structure on $MoS_2$-based electrocatalysts for water splitting

Mengmeng Liu[1,§], Chunyan Zhang[1,§], Ali Han[2,§], Ling Wang[1], Yujia Sun[1], Chunna Zhu[1], Rui Li[1], and Sheng Ye[1] (✉)

[1] College of Science & School of Plant Protection, Anhui Agricultural University, Hefei 230036, China
[2] Shenyang National Laboratory for Materials Science, Institute of Metal Research, Chinese Academy of Sciences, Shenyang 110016, China
[§] Mengmeng Liu, Chunyan Zhang, and Ali Han contributed equally to this work.



**Received:** 20 January 2022 / **Revised:** 5 March 2022 / **Accepted:** 7 March 2022

## ABSTRACT

Electrocatalytic water splitting into hydrogen is one of the most favorable approaches to produce renewable energy. $MoS_2$ has received great research attention for both hydrogen evolution reaction (HER) and oxygen evolution reaction (OER) due to its unique structure and ability to be chemically modified, enabling its electrocatalytic activity to be further enhanced or made comparable to that of Pt-based materials. In this review, we discuss the important fabrication approaches of $MoS_2$ ultrathin nanosheet ($MoS_2$ NS) to improve the intrinsic catalytic activity of bulk $MoS_2$. Moreover, several modification strategies involve either morphology modulation or electron structural modulation to improve the charge transfer kinetics, including doping, vacancy, and heterojunction construction or single-atom anchor. Our perspectives on the key challenges and future directions of developing high-performance $MoS_2$-based electrocatalysts for overall water splitting are also discussed.

## KEYWORDS

$MoS_2$, morphology, electronic structure, electrocatalysis, water splitting

## 1 Introduction

With the increasing attention to environmental pollution and energy crisis, developing sustainable and clean energy is the focus of current research [1]. Hydrogen has been intensively studied due to its high energy density and zero carbon emission [2–4]. Electrocatalytic water splitting is one of the most feasible methods to produce hydrogen including two half reactions: hydrogen evolution reaction (HER) by cathode and oxygen evolution reaction (OER) by anode. Due to the requirements of high thermodynamic reaction barriers in a four-electron multistep reaction process [5, 6], OER is currently at a bottleneck stage. Noble metal based electrocatalysts are usually used for electrocatalytic reaction due to the excellent electrocatalytic performance [7–9]. However, the scarcity and high cost of noble metal limit their wide application [10, 11]. Therefore, it is of great significance to develop electrocatalysts for water splitting with low cost, abundant reserves, and high catalytic efficiency [12].

At present, the researches of non-noble metal-based catalysts such as oxides [13, 14], hydroxides [15, 16], sulfides [17–19], phosphides [20, 21], and carbides [22–26] have attracted extensive attention. In particular two-dimensional (2D) layered structure $MoS_2$ has become a promising catalyst for electrocatalytic water splitting due to the adjustable band gap and strong electron acceptance ability [27, 28]. However, the high overpotential and poor stability in OER have become the bottleneck restricting the development of $MoS_2$-based electrocatalysts. Therefore, it is very important to optimize the electrocatalysts for water splitting.

Various approaches have been used to improve the intrinsic activity of $MoS_2$ [29]. The $MoS_2$ nanosheets with controllable morphology and size can be synthesized by hydrothermal method [30]. High-purity $MoS_2$ films can be prepared by chemical vapor deposition (CVD) [31] and form a unique structure coupled with other catalysts. Bulk $MoS_2$ is stripped by liquid phase exfoliation [32] and chemical exfoliation [33, 34] to obtain $MoS_2$ nanosheets with rich edge active sites. Through the morphology modulation, the $MoS_2$ electrocatalysts are optimized at nanoscale to achieve high catalytic performance. In particular, Janus [35, 36], hollow [37–39], core–shell [40], and yolk–shell [41–43] structures assembled by nanosheets have been constructed, which can enhance the mechanical strength to improve the stability of the catalysts and promote charge transfer in catalytic reaction [44].

Researches indicate that the catalytic activity of $MoS_2$ originates from the active edge sites due to the catalytic inertia of basal plane [45–48]. Electronic structure modulation including vacancies [49, 50], doping [51–53], heterostructure construction [54–58], and single atom catalysts [59–61], can activate inert basal planes to enhance catalytic activity. It is worth noting that modulating the electronic structure can enhance the conductivity of $MoS_2$, adjust the charge distribution of the coordination atoms, and make the interfacial charge rearrange to promote the adsorption and desorption of H* and oxygen-containing intermediates, which has become an important approach for improving water splitting performance of $MoS_2$-based electrocatalysts [62].

In this review, we summarize the fabrication strategies of $MoS_2$-based electrocatalysts, and discuss the effect of morphology structures including Janus, hollow, core–shell, and yolk–shell on physical and chemical properties. In addition, the electronic

Address correspondence to sye503@ahau.edu.cn

structure of $MoS_2$ is also modulated via doping, the construction of vacancy and heterojunction, and single atom anchor. The development and challenges of $MoS_2$-based electrocatalysts for overall water splitting are prospected.

## 2 Fabrication strategies of $MoS_2$ ultrathin nanosheets ($MoS_2$ NSs)

In the era of new energy, it is very urgent to develop efficient and high-active HER/OER catalysts. As one of the first earth-abundant catalysts, $MoS_2$ with low cost has been proved to be a promising catalyst for electrochemical water splitting [43, 63, 64]. Currently, many approaches have been employed to prepare $MoS_2$ NSs to improve the intrinsic catalytic activity of bulk $MoS_2$, such as hydrothermal synthesis, CVD, liquid phase exfoliation, and chemical exfoliation (Fig. 1).

### 2.1 Hydrothermal synthesis

Hydrothermal synthesis is a kind of commonly used liquid chemical synthesis technology, which mainly configures the raw materials into a uniform solution with water as solvent in a high-pressure reactor. It has the advantages of high purity, good dispersion, and controllable particle size, and has been widely used in the preparation of inorganic materials, biological materials, and geological materials.

In the hydrothermal synthesis process, metal sulfides with various morphologies and structures can be synthesized by changing solvents, surfactants, and other additives [65]. High-quality $MoS_2$ nanosheets with controllable morphology and size can be prepared by hydrothermal synthesis. Pan and his colleagues prepared N and P co-doped $MoS_2$ array on the carbon cloth (NP-$MoS_2$/CC) by ammonia ions-guided-nitrogenization-phosphorization as the self-supported electrode to efficiently catalyze HER in a wide pH range (Fig. 2(a)) [66]. X-ray diffraction (XRD) patterns show that all peaks matched with the 2H-$MoS_2$, indicating that doping N and P did not change the 2H-$MoS_2$ phase structure (Fig. 2(c)). The scanning electron microscopy (SEM) shows that the surface of carbon cloth is completely covered by crosslinked nanosheets with a mean size of 200–400 nm (Fig. 2(b)). The NP-$MoS_2$/CC has a specific surface area of 40 $m^2 \cdot g^{-1}$, which has rich mesoporous structure to speed up $H_2$ transport. There is a strong chemical interaction between Mo–N and Mo–P bonds, which corresponds to the Mo–N–P site in NP-$MoS_2$ (Figs. 2(d) and 2(e)). Xie's team prepared defect-free and defect-rich $MoS_2$ nanosheets via hydrothermal synthesis [67]. The defect-free $MoS_2$ nanosheets were prepared by placing a mixture containing a high level of hexaammonium heptamolybdate precursor and a small amount of $CH_4N_2S$. Thicker $MoS_2$ nanosheet assemblies can be obtained by reducing the concentration of precursor and adding excess $CH_4N_2S$. The defect-free $MoS_2$ nanosheets not only exhibit ultrathin morphology and slight assembly characteristics, but also have high crystallinity and single crystal characteristics. SEM shows that the thicker nanosheet assemblies with poor dispersibility and a few microns in size are composed of many thicker nanosheets with a size of hundreds of nanometers. It can be seen that high precursor concentration is the key to stabilizing the morphology of ultrathin nanosheets, and excessive $CH_4N_2S$ is prerequisite for the formation of defect-rich structure.

### 2.2 CVD

Due to its advantages of large growth area and high product quality, CVD becomes a major technology for preparing high purity and high-performance solid films. CVD can produce a variety of metal, alloy, ceramic, and compound precipitation coatings with unique structures via various reactions.

CVD has great advantages in preparing high-quality and uniform $MoS_2$ nanosheets with controllable size. For example, Lee's team prepared $CoS_x$@$Cu_2MoS_4$-$MoS_2$/N,S-co doped graphene ($MoS_2$/NSG) core–shell heterostructure by mixing $Co(NO_3)_2 \cdot 6H_2O$, $Cu(NO_3)_2 \cdot 6H_2O$, graphene oxide, $(NH_4)_2MoS_4$, and $CH_4N_2S$ at 80 °C [31]. The solid powder after freeze-drying was calcined in the CVD system at 500 °C in $H_2$:Ar (3:7) flow and 900 °C in Ar (Fig. 3(a)). XRD patterns reveal that $CoS_x$@$Cu_2MoS_4$-$MoS_2$/NSG was successfully prepared (Fig. 3(b)). Field emission SEM (FESEM) and transmission electron microscopy (TEM) images show a three-dimensional (3D) porous structure formed by interconnected sheet tiny hole layers (Figs. 3(c)–3(e)). The high-resolution TEM (HRTEM) image shows that the layer spacing of $MoS_2$ nanosheets is 0.62 nm and the lattice spacings of $CoS_x$ core are 0.20 and 0.28 nm. High-angle annular dark-field scanning transmission electron microscopy (HAADF-STEM) and energy

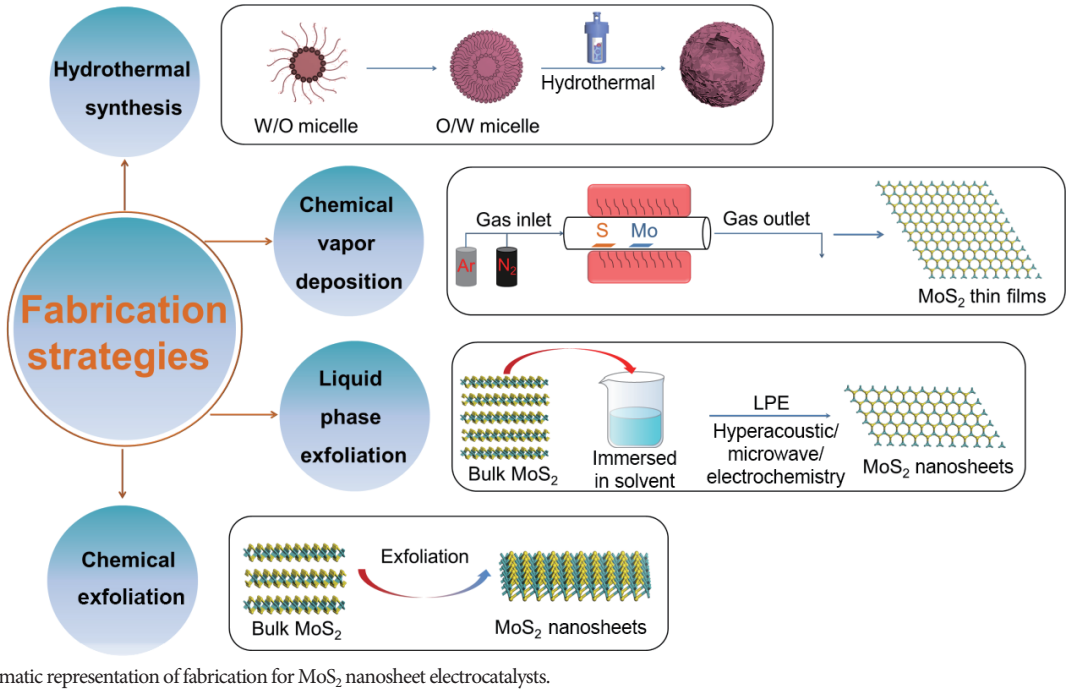


**Figure 1** Schematic representation of fabrication for $MoS_2$ nanosheet electrocatalysts.

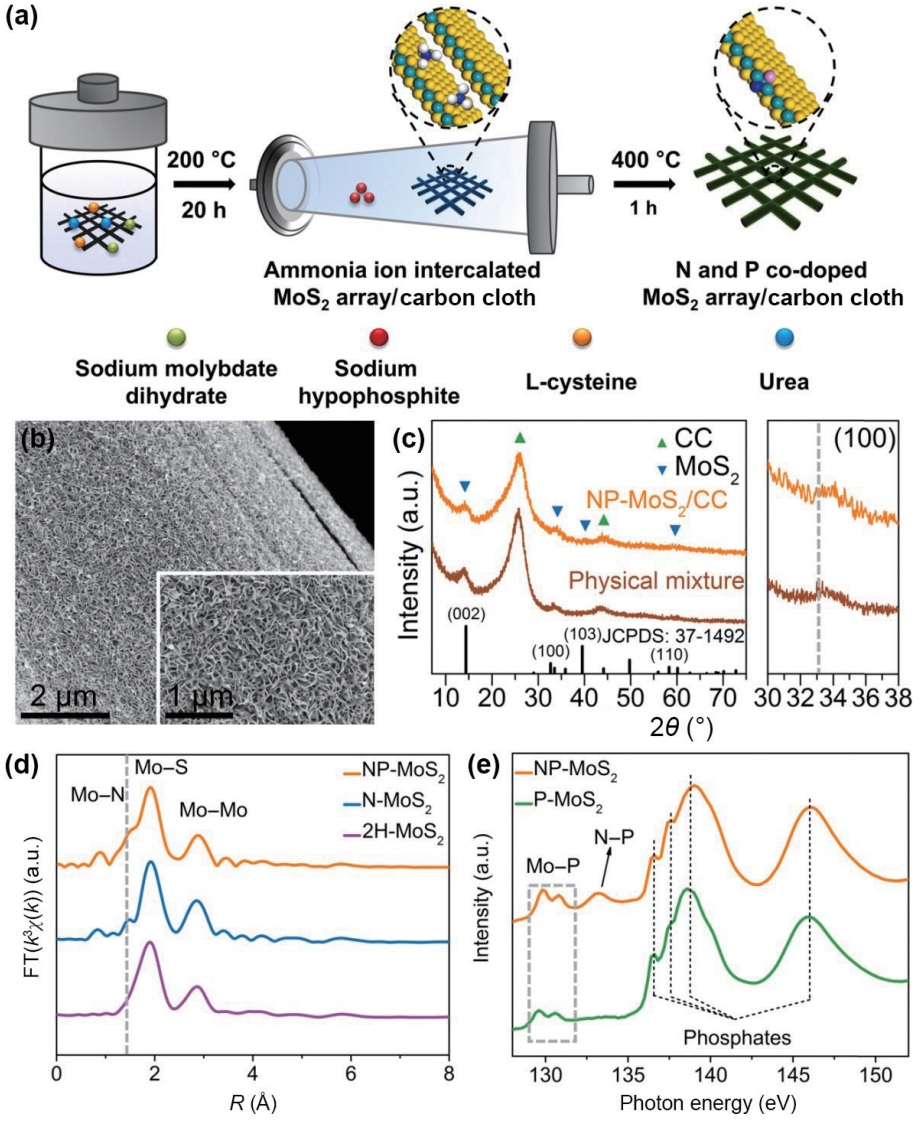


**Figure 2** (a) Schematic illustration of the synthesis process of NP-$MoS_2$/CC. (b) SEM images. (c) XRD patterns. (d) Mo K-edge Fourier transformed $k^3$-weighted extended X-ray absorption fine structure (FT-EXAFS). (e) P L3-edge X-ray absorption near edge structure (XANES). Reproduced with permission from Ref. [66], © Elsevier Ltd. 2019.

dispersive X-ray spectroscopy (EDS) mapping images reveal that N, C, Mo, S, Co, and Cu are homogeneously distributed in the core–shell heterostructure (Fig. 3(f)). $N_2$ adsorption–desorption measurement delivers that $MoS_2$/NSG demonstrates a mesoporous structure (2–50 nm) with a large specific surface area (203.6 $cm^2 \cdot g^{-1}$).

Some substances grown by CVD can form the intrinsic point defects by the wrong arrangement of the matrix atoms constituting the crystal. Garaj and his colleagues explored the method of etching $MoS_2$ nanosheets with NaClO solution [27]. It is found that the etching positions of NaClO solution have a certain relationship with the structure of $MoS_2$. Generally, the etching of $MoS_2$ crystal with NaClO solution starts from the edge with active center. However, when NaClO solution etches $MoS_2$ grown by CVD, the etching starts from the base plane accompanied by small triangular pits. The formation of intrinsic-point defects can be etched on the substrate during the growth of $MoS_2$ by CVD. Most importantly, the triangular pit can enhance the active center of $MoS_2$ and thus improve its catalytic performance. S defect engineering is one of the most important ways to improve the electrocatalytic performance of $MoS_2$ for HER, which can also be prepared by CVD. The electrocatalytic activity of the edgeless monolayer (1L) film is much higher than 1L flake, when studying the catalytic activity of the $MoS_2$ films synthesized by CVD technology [68]. The film has a large number of crystal boundaries and S vacancies, and the grain size is 30–100 nm, while the discrete sheet is 1 μm without S vacancy. In the process of CVD film synthesis, the S vacancy density is controlled by changing the temperature (700–900 °C). The film with S vacancies density in the scope of 7%–10% has the highest catalytic activity.

### 2.3 Liquid phase exfoliation

Liquid phase exfoliation has been developed rapidly in recent years, which can realize industrial production and is very suitable for the preparation of composite materials. The preparation of a material by stripping needs to overcome the van der Waals force between the matrix material layers, and dispersing the matrix in liquid is the most direct and effective way to reduce the van der Waals force.

The liquid phase exfoliation has the advantages of simple process, high product quality, and low preparation temperature. Black phosphorus quantum dots (BP QDs) and $MoS_2$ nanosheets were prepared by liquid phase exfoliation. Then, they were sonicated for 5 min and centrifuged at 18,000 rpm for 10 min to obtain BP/$MoS_2$ composites [69]. TEM images show that the diameter of BP QDs is about 2–6 nm. In addition, the atomic

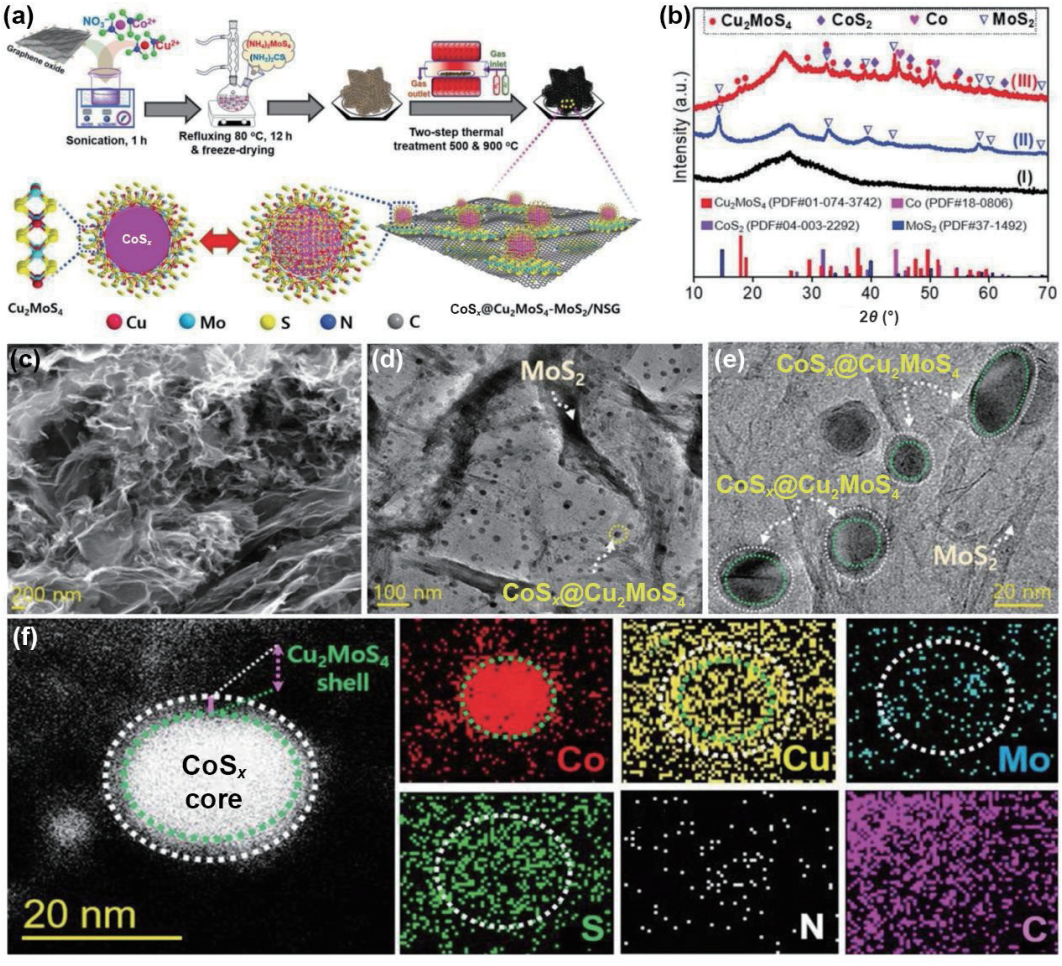


**Figure 3** (a) Schematic showing the preparation of $CoS_x$@$Cu_2MoS_4$-$MoS_2$/NSG composite. (b) XRD patterns. (c) FESEM image. (d) and (e) TEM and HRTEM images. (f) HAADF-STEM and EDS elemental mapping images of $CoS_x$@$Cu_2MoS_4$-$MoS_2$/NSG. Reproduced with permission from Ref. [31], © WILEY-VCH Verlag GmbH & Co. KGaA, Weinheim 2020.

force microscopy (AFM) images display that the mean thickness of pure $MoS_2$ nanosheets is about 3.5 nm, while the thickness of BP QDs spread on the outside of $MoS_2$ nanosheets is about 1.2 nm. The electrochemical impedance spectroscopy (EIS) curves of the samples demonstrate that the charge transfer resistance ($R_{ct}$) of BP QDs/$MoS_2$ complex material is less than that of pure $MoS_2$ and BP QDs, indicating the charge transfer speed of BP QDs/$MoS_2$ composite is fast and has a good catalytic reaction kinetic process.

It is very important to prepare $MoS_2$ composite materials with high-density active edge position. Wu et al. prepared $MoS_2$ NSs with good water solubility and rich defects via low-temperature liquid phase exfoliation [32]. The massive $MoS_2$ powder is dissolved in a mixed solution containing $NaBH_4$ after liquid nitrogen pretreatment (Fig. 4(a)). $MoS_2$ NSs show larger fragments than defect-rich $MoS_2$ NSs (d-$MoS_2$ NSs). The transverse size of d-$MoS_2$ NSs is reduced to tens to hundreds of nanometers, and the thickness is reduced to about 1.5 nm, which is mainly caused by the action of $NaBH_4$ (Fig. 4(b)). The AFM image shows that the hole increases with time until the nanosheets are broken into smaller fragments. The results demonstrate that d-$MoS_2$ NSs with high density, active edge position, and water solubility can be prepared by liquid phase exfoliation method. The d-$MoS_2$ NSs deliver outstanding catalytic performance, as well as long-term stability for HER (Fig. 4(c)).

## 2.4 Chemical exfoliation

Because of low cost and high efficiency, chemical exfoliation technology has gradually become the most effective way to prepare high-quality 2D materials with good crystal structure in large quantities. The synthesis of $MoS_2$ nanostructures can be controlled by simple intercalation chemistry. Li intercalation exfoliation is particularly important in the chemical exfoliation [70]. Next, we mainly introduce the chemical exfoliation of $MoS_2$ nanostructures by Li intercalation.

Li was inserted between the layers of $MoS_2$ and reacted violently with water, which not only led to the generation of hydrogen between the crystal layers, but also promoted the separation of $MoS_2$ layers. By controlling the nanostructure and crystal form of $MoS_2$, the conductivity and density of active centers can be improved. Jin's group synthesized $MoS_2$ nanosheets through simple intercalation [33]. The glass substrate covered with $MoS_2$ nanostructures was immersed in n-butyl Li solution at 60 °C, and then stripped by the reaction of intercalated Li with excess water. Powder XRD patterns show that $MoS_2$ nanostructures are effectively exfoliated into basically single layers (Fig. 5(d)). Interestingly, the Li intercalation exfoliation can make the $MoS_2$ nanostructure change from 2H-$MoS_2$ to 1T-$MoS_2$, while the morphology of the exfoliated nanosheets won't be changed (Figs. 5(a)–5(c)). EIS displays that $R_{ct}$ of 1T-$MoS_2$ is much smaller than that of the $MoS_2$ nanostructures, indicating 1T-$MoS_2$ substantially boosts electron-transfer kinetics.

Qiao's research group soaked massive $MoS_2$ powder in n-butyl Li solution to prepare $MoS_2$ nanosheet and 2D Co-metal-organic framework (MOF)/$MoS_2$ nanosheet successively by chemical exfoliation with simple ultrasonic assisted solution method (Figs. 5(e) and 5(f)) [34]. The SEM images show the Co-MOF/$MoS_2$ samples with several microns of transverse size and flake morphology with ripples and wrinkles on the outside of the

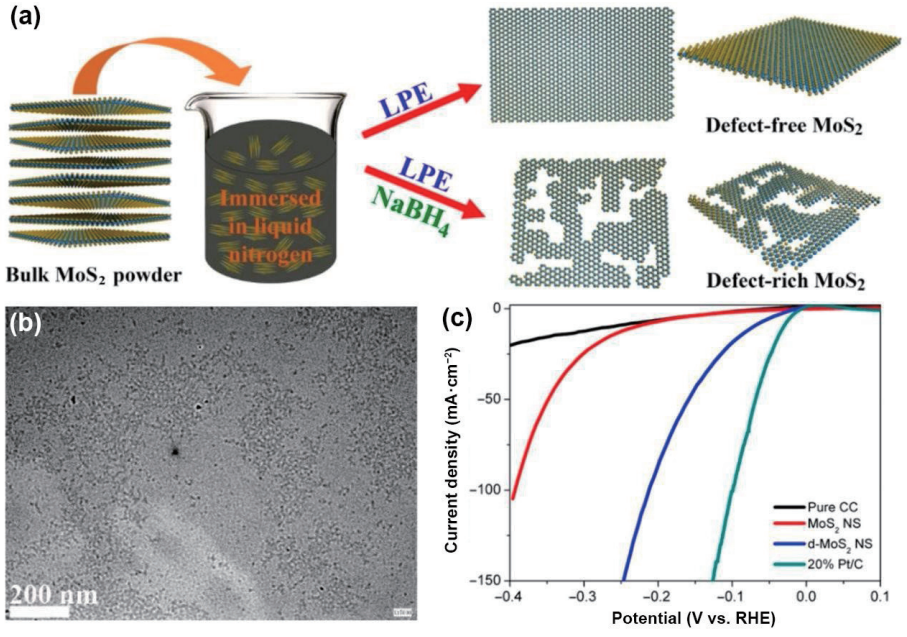


**Figure 4** (a) Schematic illustration of the synthesis process of cryo-mediated liquid phase exfoliation. (b) TEM image. (c) Polarization curves. Reproduced with permission from Ref. [32], © American Chemical Society 2019.

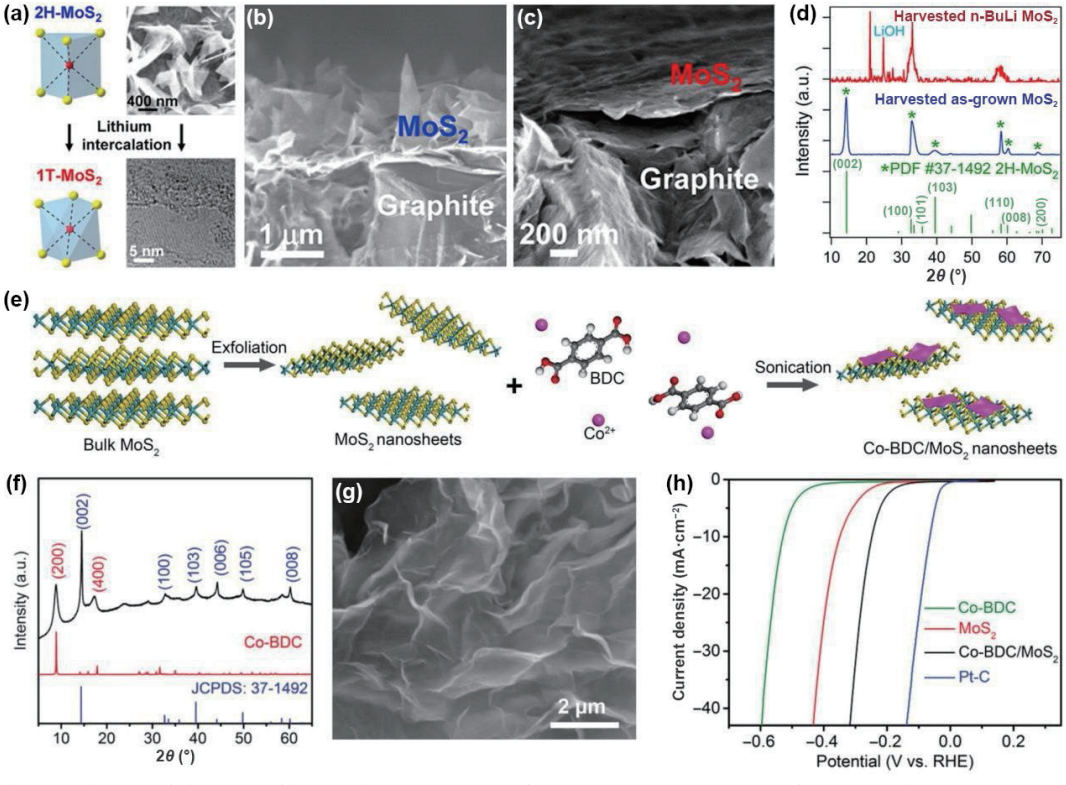


**Figure 5** (a) Schematic diagram of chemical exfoliation. (b) FESEM image of 2H-$MoS_2$. (c) FESEM image of 1T-$MoS_2$. (d) XRD patterns. Reproduced with permission from Ref. [33], © American Chemical Society 2013. (e) Schematic of the synthesis process for Co-BDC/$MoS_2$ nanosheets. (f) XRD patterns. (g) FESEM image. (h) Polarization curves. Reproduced with permission from Ref. [34], © WILEY-VCH Verlag GmbH & Co. KGaA, Weinheim 2019.

exfoliated $MoS_2$ sample (Fig. 5(g)). X-ray photoelectron spectroscopy (XPS) spectra reveal the partial phase transition of $MoS_2$ from 2H phase to 1T phase after Co-MOF is deposited on $MoS_2$ nanosheets. The high conductivity of 1T $MoS_2$ enhances the HER performance (Fig. 5(h)). Similarly, the transformation from 2H-$MoS_2$ to 1T-$MoS_2$ after chemical exfoliation is also mentioned in the report of Xia's research group on the active system of Au/$MoS_2$ for HER. 1T-$MoS_2$ can activate the inert plane of $MoS_2$, produce more catalytic active sites, and has excellent electronic conductivity.

## 3 Morphology modulation of $MoS_2$ assemblies for water splitting

2D structure tends to accumulate during the catalytic process and reduces the catalytic activity. Therefore, it is necessary to optimize the catalyst at nanoscale via morphological modulation to stabilize the catalytic performance (Table 1). The 3D structures such as Janus, hollow, core–shell, and yolk–shell can enhance the mechanical strength of the catalyst to improve the stability of the catalyst and promote the charge transfer (Fig. 6).

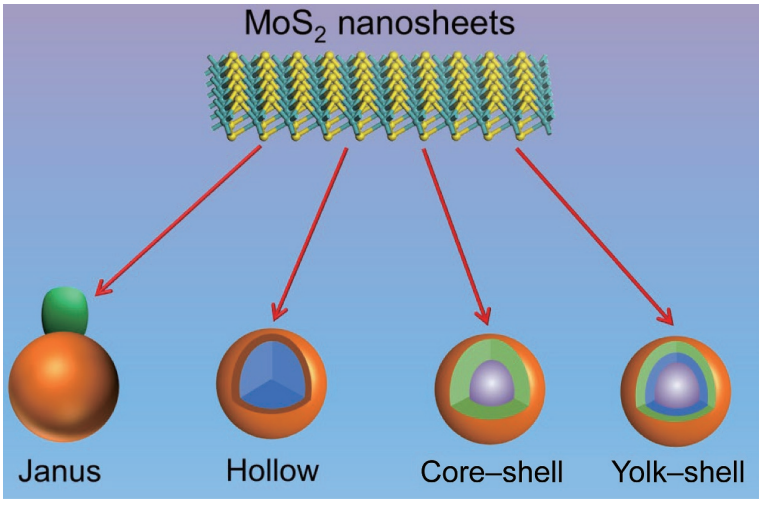


**Figure 6** Schematic representation of morphology modulation of $MoS_2$ assemblies.

### 3.1 Janus

As an emerging class of nanostructures having two faces, Janus structure is a kind of charming nanomaterials for promising applications in various areas. Some nanomaterials with asymmetric heterostructures on the nanoscale can provide many incredible properties that cannot be achieved in uniform or symmetric nanomaterials. Researchers have designed a lot of strategies to synthesize different Janus nanoparticles.

Wang et al. utilized $MoS_2$ as hydrophobic layer and ZnO as anticorrosion layer to prepare a novel multifunctional Janus-type thin film on the surface of Al, which has hydrophobic and anticorrosion properties [71]. Janus-type membranes can simultaneously prevent the intrusion of excess water molecules and hydroxide ions. Zhang et al. prepared Janus amphiphilic nanosheets composed of N-doped layered mesoporous carbon (NMC) and $MoS_2$ for hydrophilic side and hydrophobic side, respectively [36]. 2D NMC was synthesized with dicyandiamide and glucose as precursors. The functional groups (i.e., $-NH_2$, –COOH, and –CONH–) on the surface of the carbon layer fix the molybdate, and the NMC/$MoS_2$ carrier layer is transformed into uniform $MoS_2$ to form the Janus amphiphilic carbon layer, which shows more reliable performance and practicability.

Zhou et al. proposed a flexible method for controlling modified Au nanoparticles on solid $MoS_2$ microspheres [74]. The formation of $MoS_2$/Au Janus particles is due to the surfactant-induced aggregation and growth of Au nanoparticles on $MoS_2$ microspheres. Moreover, Lu et al. reported a synthesis strategy to grow Janus 1Ls of transition metal dihalides, breaking the symmetry of planar structure [72]. In particular, on the basis of $MoS_2$ 1L, S atoms of the top layer are substituted with Se atom completely. Large-scale preparation of such highly homogeneous Janus nanoparticles remains challenging. Zhou et al. proposed a simple wet chemistry strategy and synthesized Ag-$MoS_2$ Janus nanoparticles by adding an appropriate amount of $AgNO_3$ to an aqueous solution containing $MoS_2$ nanospheres (200 nm) (Figs. 7(a) and 7(b)) [73]. Each Janus nanoparticle consists of a tiny Ag dot modified $MoS_2$ nanoparticle and a polyhedral Ag single crystal (100 nm), which are connected to each other and present a snowman shaped dimer (Figs. 7(c) and 7(d)). Furthermore, Zhang et al. demonstrated that twist angle and interfacial composition can adjust van der Waals of interlayer coupling and charge transfer in Janus MoSSe/$MoS_2$ heterogeneous bilayers [75]. This work presents the interfacial interactions in heterostructures by exploiting the asymmetry of Janus structure.

### 3.2 Hollow

Hollow nanometal sulfides have great application in energy conversion and storage [76]. They generally have the characteristics of fast mass transfer rate, abundant active sites, large specific surface area, and high current density. Nowadays, hollow $MoS_2$ has been considered as one of the most promising water-splitting catalysts instead of noble metal Pt catalyst.

Recently, our group designed and prepared the $MoO_2$/$MoS_2$/C hollow nanoreactor with monodisperse sandwich structure, which could adjust the adsorption–dissociation barrier effectively and accelerate the water splitting rate [39]. The nanoreactors assembled by $MoS_2$ nanosheets and the Mo, S, O, and C elements are homogeneously distributed in the hollow nanoreactor (Figs. 8(a)–8(c)). During HER test, the structure and components of hollow $MoO_2$/$MoS_2$/C nanoreactors do not change. The results show that the prepared 3D hollow structure catalyst presents superior stability.

The $MoS_2$ micro/nanoboxes have superior electronic and ionic conductivity. Lou et al. synthesized hollow $MoS_2$ microboxes using uniform $MnCO_3$ microcubes via template-assisted method [77]. MnS is changed from $MnCO_3$ template in order to constitute MnS@$MoS_2$ core–shell microcubes in the hydrothermal process, which can be selectively dissolved in HCl solution to obtain the hierarchical $MoS_2$ microboxes. The EIS reveals that the hierarchical $MoS_2$ microboxes exhibited much lower resistance than bulk $MoS_2$. The FESEM images show that the $MoS_2$ microboxes possess a hollow interior with a hollow cavity about 2.5 μm. Interestingly, doping N into carbon shell can provide more active sites for electrochemical reaction and further improve the conductivity of the composite structure. On this basis, Lou's group further developed a hollow hybrid structure of N-doped carbon nanoboxes loaded ultrathin nanosheets [38]. The $Fe_2O_3$ nanocubes with the thickness of about 40 nm and an average size of about 500 nm are coated with even and glazed polydopamine (PDA) to form a core–shell structure of $Fe_2O_3$@PDA nanocubes. The $Fe_2O_3$@PDA nanocubes are carbonized in $N_2$ and converted to $Fe_3O_4$@C nanocubes which can be dissolved by HCl to obtain carbon nanoboxes. The electrical conductivity of carbon nanoboxes with short diffusion length of electron ions modified with N can be remarkably improved and $MoS_2$ aggregation can be effectively prevented. The FESEM images exhibit that the C@$MoS_2$ nanoboxes are unvaried with an average size of about 580 nm.

Converting nanocubes into nanoboxes via an unusual etching process can expose more active marginal areas (Fig. 8(d)). Ni and Co were doped into the sandwich $MoS_2$ by heating the Ni-Co

Prussian blue analogue (Ni-Co PBA) nanocubes and ammonium thiomolybdate [48]. Ni-Co PBA nanocubes with an average size of 400 nm are synthesized by modified precipitation method. An interesting structural transformation from solid to hollow nanocubes can be found. HRTEM images show that the borders of the rough Ni-Co PBA nanocubes are etched away completely over time to form the nanocubes assembled by ultrathin nanosheets (Fig. 8(e)). The TEM images indicate that the average size of Ni-Co-$MoS_2$ is 440 nm. The EDS mapping reveals that the Mo, S, Ni, and Co elements are uniformly distributed in the whole nanoboxes.

The self-supported hollow heterostructure *in situ* grown on the substrate can avoid using the polymer binders and conductive additives, which blocks the active sites and increases the resistivity. Yang et al. prepared novel hierarchical nanotube arrays of $MoS_2/CoS_2$ heterostructures as self-supported catalysts on carbon cloth via MOF interfacial engineering for pH-universal HER [78]. The $MoS_2/CoS_2$ heterostructure has a specific surface area of 277.9 $m^2 \cdot g^{-1}$ with the pore size concentrated in the range of 1 to 2 nm. The hollow structure provides rich electrolyte reachable locations and high mass transfer rates, resulting in a low overpotential of 150 mV and small Tafel slope of 66.1 $mV \cdot dec^{-1}$. 3D layered heterostructures supported by multi-walled carbon nanotubes can further optimize the hollow structure by reducing the accumulation of $MoS_2$ nanosheets [79]. Yang and co-workers prepared a ternary composite MCNTs@$CoS_x$@$MoS_2$ with 3D hollow structure by a two-step solvothermal method, which exhibits good durability in both acidic and alkaline solutions [80]. The MCNTs@$CoS_x$@$MoS_2$ has a diameter of 135 nm and the thickness of $MoS_2$ nanosheets is about 15 nm. The HRTEM images prove the existence of Mo vacancies, which can effectively adjust the band gap width and improve the resistivity of $MoS_2$. The ternary MCNTs@$CoS_x$@$MoS_2$ catalyst shows a low overpotential of 196 mV for HER and 285 mV for OER, better than binary MCNTs@$Co_9S_8$, MCNTs@$MoS_2$, and $CoS_x$@$MoS_2$ [80–82].

Introducing macro/micro/meso pores into the shell material is an effective approach to increasing the variation of electrolyte to the inner void. Kim et al. prepared the hollow Co,Nb-$MoS_2/TiO_2$ heterostructure by adding Co and Nb to $MoS_2$ NSs grown on $TiO_2$ hollow microspheres [37]. The synergistic effect of hollow spherical structure and heterostructure between $MoS_2$ shell and $TiO_2$ core provides an effective channel for electron conveyance and exposes more space for ion diffusion. The average diameter of Co,Nb-$MoS_2/TiO_2$ heterostructure is about 480 nm, with a core of 390 nm $TiO_2$ and a shell of 45 nm Co,Nb-$MoS_2$ layer. The Co,Nb-$MoS_2/TiO_2$ heterostructure has a specific surface area of 198.8 $m^2 \cdot g^{-1}$ and the pore size ranges from 1.9 to 2.5 nm, showing a superior activity with a low overpotential of 58.8 mV for HER and 260.0 mV for OER.

### 3.3 Core–shell

Core–shell structure $MoS_2$ has been widely applied in electrocatalytic water splitting, due to the advantages including large electrochemical contact surfaces, good flexibility, ultrahigh specific surface area, and hierarchical interconnected pore network. The construction of core–shell nanostructures is an important and attractive approach to regulate the electronic properties and geometric structure of $MoS_2$ electrocatalysts.

It is an effective way to realize high active electrocatalysts by constructing heterostructures in core–shell $MoS_2$. Yamauchi et al. prepared the core–shell $Co_3S_4$@$MoS_2$ heterostructure for water splitting via a two-step hydrothermal reaction (120 °C for 6 h; 200 °C for 12 h). The structure was formed *in situ* on the surface of $Co_3S_4$ nanoboxes by the growth of $MoS_2$ nanosheets, and it could easily release the bubbles formed on the surface of the electrode to prevent the catalyst from falling off the electrode. The

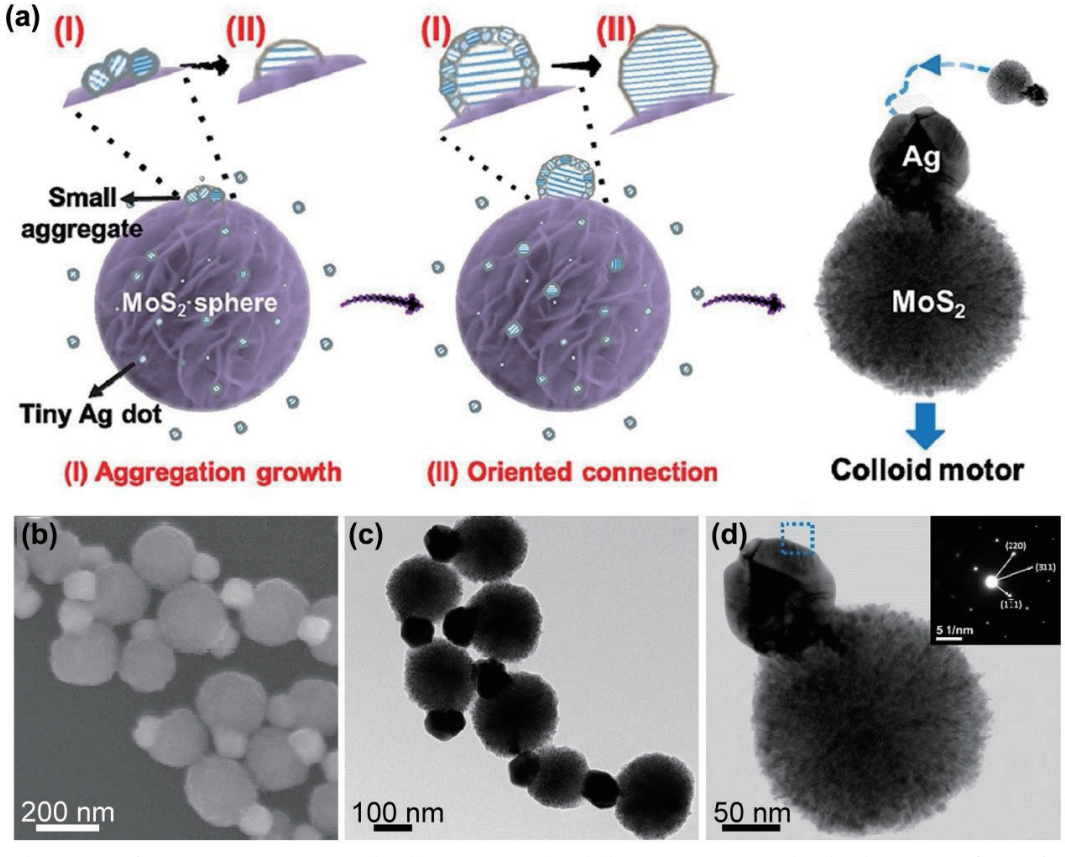


**Figure 7** (a) Synthetic process for Ag-$MoS_2$ Janus nanoparticles. (b) SEM image. (c) and (d) TEM images. Reproduced with permission from Ref. [73], © American Chemical Society 2019.

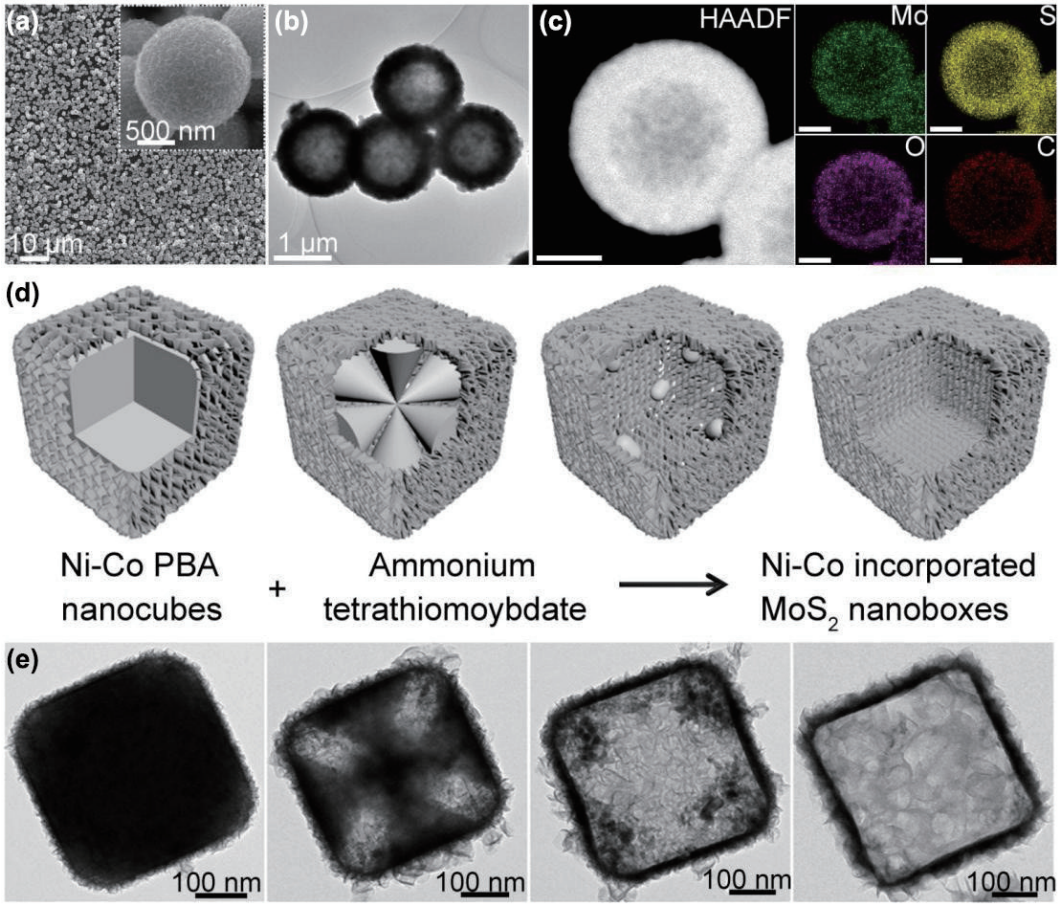


**Figure 8** (a) FESEM images, (b) TEM image, and (c) HAADF-STEM and EDS elemental mapping images of $MoO_2/MoS_2/C$. Reproduced with permission from Ref. [39], © Wiley-VCH GmbH 2021. (d) Schematic illustration of the formation process of Ni-Co-$MoS_2$ nanoboxes and (e) TEM images of the as-synthesized products obtained at different time intervals. Reproduced with permission from Ref. [48], © WILEY-VCH Verlag GmbH & Co. KGaA, Weinheim 2016.

synergistic effect makes $Co_3S_4@MoS_2$ heterostructure possess superior electrocatalytic activity with a low overpotential of 280 mV for OER and 136 mV for HER at 10 $mA·cm^{-2}$ in alkaline solution. The heterostructures show different size-dependent HER performance and much lower Tafel slopes than pure $MoS_2$ nanosheet [83]. On the basis, a 1L $MoS_2$ coated polyhedron Ag core–shell heterostructure $Ag@MoS_2$ was synthesized via wet chemical synthesis method. The formation of S–H bonding indicates that the S atom is HER catalytic active site [40]. Nowadays, the researchers are looking for a reasonable solution to the limitation of terminal active sites. Chen et al. constructed $Au@MoS_2$ heterostructure to address the poor electrical conductivity of the supporting substrate, which provides abundant end-to-end active sites. The HRTEM reveals that the plane atomic structure of $MoS_2$ is typical hexagonal, and the layer spacing of wings is 0.65 nm. The key advantage of this technique is the ability to grow highly controlled independent $MoS_2$ wings with ideal morphology, which leads to an abundance of edge-terminated active sites to drive hydrogen molecules formation, and the ability to achieve efficient charge transfer in the $Au@MoS_2$ structure [84]. Furthermore, Lee et al. fabricated a core–shell $CoS_x@Cu_2MoS_4$-$MoS_2$/NSG heteronetwork. Both TEM and AFM images show that $MoS_2$/NSG has a mesoporous structure in the range from 10 to 40 nm, which is also confirmed by $N_2$ adsorption–desorption measurements. $MoS_2$/NSG has a specific surface area of 203.6 $cm^2·g^{-1}$, and its pore sizes range from 10 to 40 nm, which shows a low overpotential of 118.1 mV for HER and 351.4 mV for OER at 10 $mA·cm^{-2}$. The superior performance is due to the rational combination of highly active core–shell $CoS_x@Cu_2MoS_4$ with a large-area and high-porosity $MoS_2$/NSG, resulting in multi-active center integration and synergistic effect [31].

Adjusting surface strain is a new strategy to significantly change the lattice parameter, the intrinsic interatomic distances, and the energy levels of the bonding electrons. Guo et al. proposed a new method that can accurately adjust the surface tension of $Co_9S_8@MoS_2$ core–shell nanocrystals, thus improving HER activity by controlling the number of $MoS_2$ shells, manipulating the hydrogen adsorption energy and kinetic barrier of the transition state 2H* (Fig. 9(a)). The $MoS_2$ demonstrates 2D nanoplate morphology, while the $Co_9S_8$ has an octahedral structure. The results indicate the $Co_9S_8@MoS_2$ core–shell nanocrystals have a large tensile surface strain of 3.5%, which can produce an optimized band gap and allow favorable hydrogen adsorption and rapid diffusion, yielding the best $\Delta G_H$ of –1.03 eV and $\Delta G_{2H^*}$ of 0.29 eV [85]. The heteroepitaxial coverage extent of $MoS_2$ shell on $Co_9S_8$ surfaces can be tuned by changing the graphitization temperatures (600–1,000 °C) (Figs. 9(b)–9(e)). Similarly, Du et al. described a novel class of $Co_9S_8@MoS_2$ core–shell structures which formed on carbon nanofibers with cubic $Co_9S_8$ as the core and layered $MoS_2$ as the shell. The sizes of the $Co_9S_8$ cores range from 20 to 100 nm, while $MoS_2$ shells have a thickness range from 4 to 8 nm with a total of 5–12 layers. In the interfacial region between $MoS_2$ and $Co_9S_8$ nanocrystals, electrons are transferred through the intermediate S atoms bonded to two metals. Meanwhile, the carbon nanofiber substrate hosts the formation of $Co_9S_8@MoS_2$, protects the electrolyte erosion, and ensures charge transfer between the electrode and $Co_9S_8@MoS_2$ [86]. Lee et al. used single-atom Co decorated $MoS_2$ nanosheets assembled on TiN nanorod arrays to prepare single-atom Co-decorated (CoSAs)-$MoS_2$/TiN nanorod arrays for water splitting in pH-universal electrolytes. The CoSAs-$MoS_2$/TiN shows a low overpotential of 187.5, 131.9, and 203.4 mV at 10 $mA·cm^{-2}$ in

acidic, alkaline, and neutral conditions, respectively, which is better than most non-precious metal HER electrocatalysts previously reported. Atomic dispersion of Co achieves maximum atomic exposure and significantly increases active Co site density. More importantly, the strong interaction between CoSAs nanosheets and layered $MoS_2$ regulates the electron density distribution of Co and $MoS_2$, providing more catalytic active sites for reactant molecules, and improving the adsorption–desorption energy of intermediate species during hydrolyzations. In addition, both CoSAs-$MoS_2$ nanospheres on the outer surface and TiN on the inner surface act as efficient conductive channels, which are used for charge transfer and greatly enhance the reaction kinetics [87].

### 3.4 Yolk–shell

Yolk–shell nanostructure is a kind of hybrid nanomaterials comprising of a movable core located in a hollow cavity surrounded by a porous shell. Due to their unique morphological characteristics, yolk–shell nanostructure has low density, good loading capacity, and large surface area. The main difference between the yolk–shell and the core–shell structure is whether there's a cavity between the core and shell. Because of the gap between the space of core and shell in the yolk–shell nanostructure, small molecules like $C_2H_4$, hydrogen, and water can freely diffuse into the gap space through the permeable shell to be used as robust nanostructures.

The electrode assembled by yolk–shell microspheres can significantly improve the electrochemical performance of the overall water splitting. Liu et al. synthesized $MoS_2$/NiS yolk–shell microspheres by ionic-liquid assisted hydrothermal method. TEM clearly confirms the yolk–shell structure of the microspheres, with an inner shell diameter of 500–700 nm and a thin inner shell thickness of 300 nm. Notably, a NiO thin layer with a lattice spacing of 0.24 nm was observed on the NiS surface. The surface electrochemical oxidation of $MoS_2$/NiS occurred during the overextended water oxidation process and NiO layer is formed, which is responsible for the high activity of $MoS_2$/NiS toward OER [41]. In addition, Zhang et al. developed a simple self-template

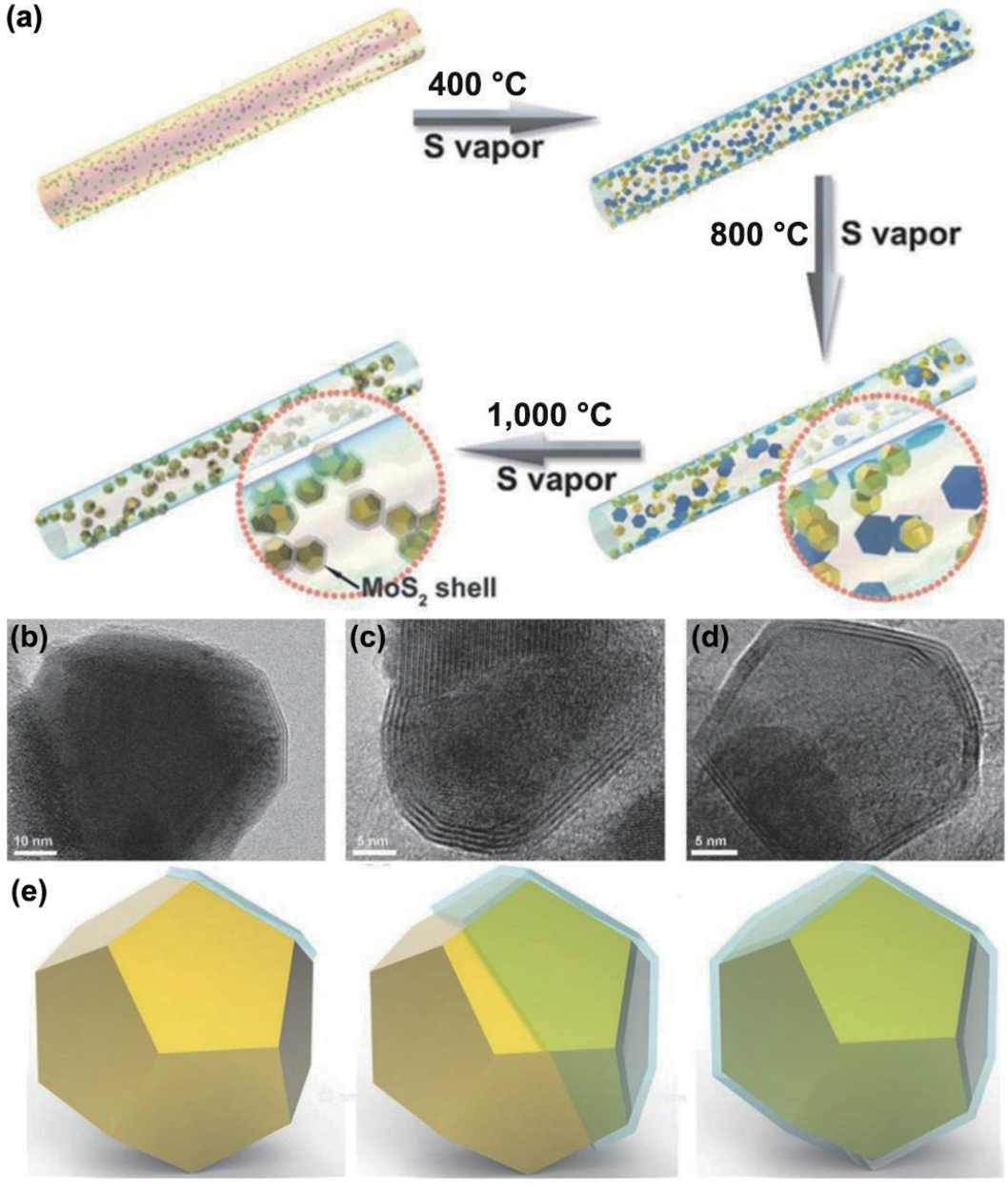


**Figure 9** (a) Synthetic process for $Co_9S_8$@$MoS_2$ core–shell nanocrystals with precisely controlled shell numbers supported on CNFs. (b)–(d) TEM images of $Co_9S_8$/1L $MoS_2$, $Co_9S_8$/2L $MoS_2$, and $Co_9S_8$/3L $MoS_2$ prepared at different graphitization temperatures of 600, 800, and 1,000 °C. (e) Schematic illustration of the structure evolutions of $Co_9S_8$/1L $MoS_2$ under different temperatures. Reproduced with permission from Ref. [85], © WILEY-VCH Verlag GmbH & Co. KGaA, Weinheim 2018.

solvothermal method of novel $MoS_2$ yolk–shell microspheres with layered porous structure. The Brunauer–Emmett–Teller (BET) specific surface area of the yolk–shell $MoS_2$ hollow spheres is as high as 252.5 $m^2 \cdot g^{-1}$, and this structure greatly increases the exposed location of active edges. The $MoS_2$ yolk–shell microspheres with hierarchical porous structure exhibit superior electrochemical properties. This method provides a new process for the synthesis of high-activity chalcogenide catalyst for HER [42].

Currently, the synthesis of the uniform and ultrafine sizes remains a major challenge. Wang et al. found a novel and simple method to synthesize the superfine $NiS_2/MoS_2$ Janus subunit organized on yolk–shell nanospheres. Due to the greatly reduced particle sizes of 2D $MoS_2$ nanosheet and one-dimensional (1D) $NiS_2$ nanoparticle, the structure largely promotes its close electron interaction and dissociation of water molecules. An average diameter of yolk–shell $NiS_2/MoS_2$ dispersed nanospheres is ~ 310 nm. The reduction of $MoS_2$ and $NiS_2$ particle size and the high-density coupling interface of bimetallic sulfide hybridization greatly promoted the tight electron interaction and dissociation of water molecules [88]. Moreover, Yang et al. synthesized $MoS_2$ nanosheets on transition metal (Co, Ni, and Fe) sulfides by solvothermal method, which showed high activity for HER/OER under alkaline conditions. The 3D open structure ensures that the high surface area of yolk–shell $MoS_2$ is 86 $m^2 \cdot g^{-1}$, which is bigger than pure $MoS_2$ (33 $m^2 \cdot g^{-1}$). The enlargement of interlayer distance and the layering of interlayer structure between $MoS_2$ shell and transition metal sulfides yolk is the main reason for improving the performance.

Recently, our group prepared monodisperse and uniform yolk–shell $MoS_2$ nanoreactor assembled by nanosheets via an oil-water microemulsion method [43]. The S vacancies introduced by O doping can be used to guide the Pt anchoring on $MoS_2$ surface to generate uniform nanoparticles, and Mo, S, O, and Pt presented homogeneous distribution (Figs. 10(a)–10(d)). The anchoring mechanism was investigated via electron paramagnetic resonance (EPR), XPS, and X-ray absorption fine structure (XAFS) (Fig. 10(e)). O-$MoS_2$@Pt exhibits superior OER activity, which is much better than most $MoS_2$-based catalysts and commercial $IrO_2$ in alkaline media (Fig. 10(f)). Due to the prevention of agglomeration, regulation of gas release, and enhanced mechanical stability, the yolk–shell structured $MoS_2$ nanoreactors exhibited superior stability in continuous electrocatalytic tests. *In situ* XRD, TEM, and XPS after cycling demonstrate the superior structural and compositional stability of the yolk–eggshell O-$MoS_2$@Pt (Fig. 10(g)). Yolk–shell structure plays an indispensable role in developing electrocatalysts possessing small size and highly dispersed active nanoparticles, which can simultaneously prevent deactivation and the loss of nanoparticles during the catalytic process.

## 4 Electronic structure modulation of $MoS_2$ electrocatalysts for water splitting

$MoS_2$ with adjustable band gap, high electron acceptance ability, and adjustable active sites has demonstrated numerous potentials in the fields of energy storage and conversion, which is an ideal object for high-efficiency electrocatalysts. The electrocatalytic water splitting process of $MoS_2$-based electrocatalysts can be promoted via modulating the electronic structure, such as doping, constructing vacancy and heterojunction, and single atom anchor (Fig. 11).

### 4.1 Doping

Intrinsic $MoS_2$ only exhibits catalytic activity at the edge S sites, while the abundant of S sites in the basal plane are inert and underutilized. Doping metal or heteroatom into $MoS_2$ is a way that can effectively activate the S atoms of basal plane and enhance intrinsic activity. On account of the simple synthesis technology, high yield, and superior chemical stability, chemical doping has great advantage for catalyst design. It can realize multi-scale modulation and provide more active sites for the HER/OER process (Table 2).

#### *4.1.1 Anion doping*

Xue et al. reported a type of P-doped $MoS_2$ nanosheets with enlarged interlayer as highly active electrocatalyst [93]. The experiments and theoretical calculations prove P doping can

**Table 1** The HER and OER actives of core/yolk–shell $MoS_2$-based catalysts

| Catalysts | Electrolyte | | $\eta_{10(HER)}$ (mV) | $\eta_{10(OER)}$ (mV) | Tafel$_{(HER)}$ (mV·dec$^{-1}$) | Tafel$_{(OER)}$ (mV·dec$^{-1}$) | Stability | Reference |
|---|---|---|---|---|---|---|---|---|
| | HER | OER | | | | | | |
| $CoS_x$@$Cu_2MoS_4$-$MoS_2$/NSG | 0.1 M KOH | 0.1 M KOH | 118.1 | 351.4 | 41.1 | 61.5 | Chronoamperometric stability for 33 h | [31] |
| HF-MoSP | 1.0 M KOH | — | 119 | — | 82 | — | 119 mV for 30 h | [89] |
| $Co_9S_8$@$MoS_2$ | 1.0 M KOH | 1.0 M KOH | 143 | 342 | 117 | 94 | *I–t* curve at overpotential for 10 h | [90] |
| Ag@$MoS_2$ | 0.5 M $H_2SO_4$ | — | 195.7 | — | 41.1 | — | Overpotential small change after 10,000 LSV cycles | [40] |
| $Co_9S_8$/$MoS_2$ | 0.5 M $H_2SO_4$ | — | 95 | — | 71 | — | –0.31 V for 10 h | [85] |
| $Co_3S_4$@$MoS_2$ | 1.0 M KOH | 1.0 M KOH | 136 | 280 | 74 | 43 | 1.51 V over 10 h | [83] |
| w-Au@$MoS_2$ (islands) | 0.5 M $H_2SO_4$ | — | 120 | — | 52.9 | — | Polarization curves for ~ 10 h | [84] |
| CoSAs-$MoS_2$/TiN NRs | 0.5 M $H_2SO_4$ | 1.0 M KOH | 187.5 | 340.6 | 53.5 | 81.2 | Chronoamperometric curve for 45 h | [87] |
| $MoS_2$@Ni/CC | 1.0 M KOH | — | 253 | — | 89 | — | 130 mV for 45 h | [91] |
| $Co_9S_8$@$MoS_2$/CNF | 0.5 M $H_2SO_4$ | 1.0 M KOH | 190 | — | 110 | 61 | Polarization curves for 1,000 cycles | [86] |
| YS-MoS | 1.0 M KOH | 1.0 M KOH | 359 | 178 | 76 | 35.7 | 285 mV for 32 h | [92] |
| $NiS_2$/$MoS_2$ | 1.0 M KOH | 1.0 M KOH | 135 | 293 | 82 | 102.3 | 10 mA·cm$^{-2}$ for 10 h | [88] |
| $MoS_2$/NiS | 1.0 M KOH | 1.0 M KOH | 244 | 350 | 97 | 108 | –244 mV for 43,200 s | [41] |
| O-$MoS_2$@Pt | — | 1.0 M KOH | — | 244 | — | 53 | 10 mA·cm$^{-2}$ for 24 h | [43] |

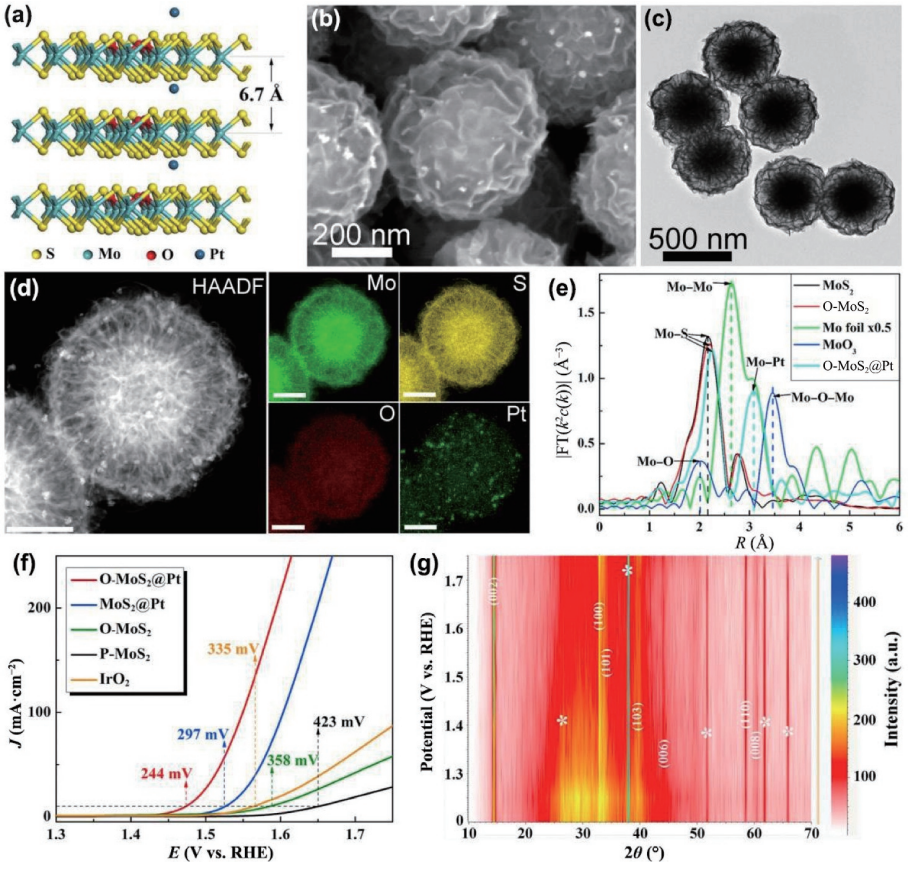


**Figure 10** (a) The crystal structure. (b) and (c) FESEM and TEM images. (d) HAADF-STEM and EDS elemental mapping images of O-$MoS_2$@Pt. (e) Mo K-edge FT-EXAFS spectra of O-$MoS_2$ and O-$MoS_2$@Pt. (f) Polarization curves. (g) The corresponding *in situ* XRD patterns at the potential from 1.3 to 1.75 V. Reproduced with permission from Ref. [43], © Elsevier Ltd. 2020.

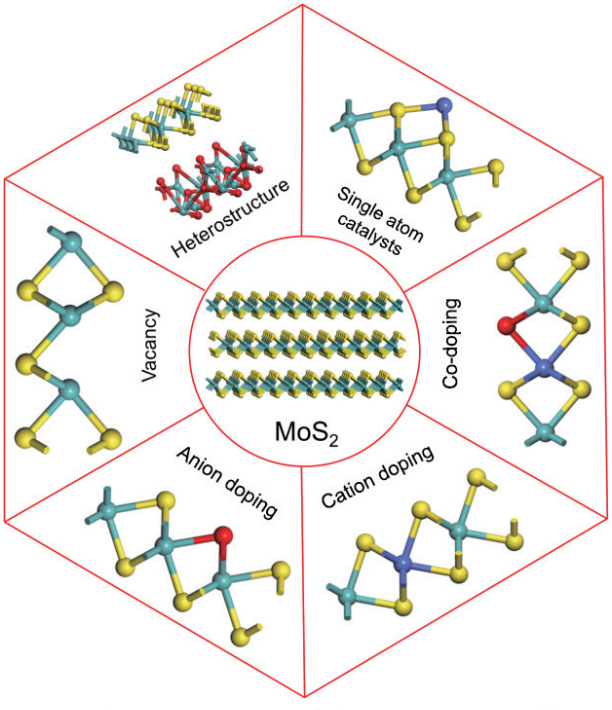


**Figure 11** Schematic representation of electronic structure modulation of $MoS_2$.

adjust the surface electronic state of $MoS_2$ to improve the intrinsic conductivity and promote electron transfer among basal plane active sites. The $\Delta G_H$ of P-doped $MoS_2$ is close to Pt, which indicates the P doping could be new active sites. Furthermore, the $\Delta G_H$ of S atoms of P-doped $MoS_2$ is reduced to 0.43 eV compared with pristine $MoS_2$ (2.20 eV), indicating the basal plane of $MoS_2$ has been activated. The interlayer spacing of P-doped $MoS_2$ nanosheets increases to 0.91 nm, indicating the enlarged interlayer can promote the hydrogen adsorption and release process. It is an ideal strategy to enhance the intrinsic conductivity and create catalytic sites of $MoS_2$. Liu and co-worker presented the concept of orbital modulation for promoting the water splitting [94]. The electronic orbital of $MoS_2$ was modulated by C-doping, resulting in enhanced HER performance in alkaline conditions. The water adsorption and dissociation of $MoS_2$ in alkaline electrolyte are poor due to the kinetic limitations. Adjusting the orbital direction of $MoS_2$ layer can improve the kinetics process. Compared with C atoms, S atoms have a larger radius, more electrons, fewer empty orbitals, and higher energy. The S atoms in $MoS_2$ are partially replaced by C atoms, resulting in $sp^2$ hybridization sites in the outermost layer of $MoS_2$. The $sp^2$ hybridization site generates a p orbital perpendicular to the basal plane, which promotes water adsorption and activation. The experiments and density functional theory (DFT) also prove that the modulation of surface orbital orientation through C doping promotes the water adsorption and dissociation.

As a typical 2D transition metal sulfide, the 2H-$MoS_2$ is widely used in catalytic reactions. The researches reveal that the electrocatalytic activity and kinetics of $MoS_2$ are closely related with phase composition. The 2H-$MoS_2$ is a stable phase and easy to prepare. However, owing to the low conductivity, the application of 2H-$MoS_2$ in electrochemical energy storage and conversion is limited. The 1T-$MoS_2$ exhibits metallic characteristics and strong charge transfer ability, which can significantly improve the electrochemical performance. Nevertheless, the synthesis of 1T-$MoS_2$ is very difficult and the 1T-$MoS_2$ can convert spontaneously into 2H phase. Xia's group

reported a strategy by using N-doped and $PO_4^{3-}$ intercalation to induce the transition from 2H-$MoS_2$ to 1T-$MoS_2$ [95]. Binder-free arrays for HER are formed through the rational bonding of (N, $PO_4^{3-}$)-$MoS_2$ nanosheets with conductive vertical graphene (VG) frameworks (Figs. 12(a)–12(c)). The unique structure of (N, $PO_4^{3-}$)-$MoS_2$/VG enhances the reaction kinetics and exhibits low overpotentials and excellent stability (Figs. 12(d)–12(f)). The scattering mechanism of the synergistic phase transition from 2H to 1T phase is proposed, and the process is confirmed by synchrotron radiation and spherical aberration TEM. Compared with 2H-$MoS_2$, $PO_4^{3-}$-$MoS_2$, N-$MoS_2$, and 1T-$MoS_2$, (N, $PO_4^{3-}$)-$MoS_2$ shows the smallest band gap (0 eV). The band gap calculation results indicate that 2H-$MoS_2$ and $PO_4^{3-}$-$MoS_2$ are indirect band gap semiconductors, and N-$MoS_2$, 1T-$MoS_2$, and (N, $PO_4^{3-}$)-$MoS_2$ are metal-like semiconductors with superior electrical conductivity (Fig. 12(g)). It is found that N-doping is the main factor for inducing the phase transition of $MoS_2$, and the coordination with $PO_4^{3-}$ significantly enhances the conductivity of the catalyst. The d-band center suggests that more antibonding states in (N, $PO_4^{3-}$)-$MoS_2$ can greatly facilitate hydrogen adsorption–desorption on the surface of catalysts. The metallic nature, the lowest frequency band center, and the smallest hydrogen adsorption–desorption energy of (N, $PO_4^{3-}$)-$MoS_2$ greatly enhance the catalytic activity. Doping and intercalation-induced phase transitions afford a new strategy for the construction of high-performance $MoS_2$ electrocatalysts.

Yang's group prepared stable 1T-$MoS_2$ with S vacancy and P doping [96]. The stable P-containing metallic 1T-$MoS_2$ nanosheets were grown *in situ* on N, P, and S co-doped hierarchical carbon microflower (P-$MoS_2$@HCMF) via dopamine self-polymerization, molybdate reduction, and hydrothermal reduction. Ammonium dihydrogen phosphate and ammonium in $CH_4N_2S$ are used as intercalator to induce the distortion of S atoms on the surface of P-$MoS_2$@HCMF. The intercalators promote the transition from 2H to 1T phase and create a certain number of S vacancies. The coupling effect of metallic phase, defect properties, heteroatom doping, and high electrical conductivity of carbon supports endow P-$MoS_2$@HCMF with superior catalytic performance. The results show that 1T phase of P-$MoS_2$@HCMF is maintained and exhibits superior stability during the HER process, indicating that P-$MoS_2$@HCMF has great potential as an efficient and stable noble metal-free electrocatalyst.

#### 4.1.2 *Cation doping*

The localized electron of $MoS_2$ redistributes due to different radius and electronic configuration of doped atoms. The redistribution of electrons is conducive to the charge transfer from the electrode to the adsorbed reactant, promoting the catalytic reaction.

The electronic conductivity and active center density of $MoS_2$ need to be improved. Jiang et al. reported a method of doping Pd atoms into the Mo sites and inducing the formation of S vacancies. Meanwhile the stable 1T-$MoS_2$ was obtained and the basal plane was activated [97]. The experimental and theoretical calculation prove that the stable 1T-$MoS_2$ with a large number of S vacancies, leading to the superior HER performance. The Pd doping reveals a positive effect on the activation of $MoS_2$ but excessive Pd doping decreases the HER performance. However, Pd atoms could introduce S vacancy and activate the $MoS_2$ basal plane by activating adjacent S atoms. The excessive concentration of Pd and S vacancy would decrease the site density of Pd–S–Mo, and affect HER performance. Pd doping leads to the 1T-$MoS_2$ more stable than 2H-$MoS_2$ owing to the high stability of the Pd–S bond.

Adjusting the energy level of electrocatalyst is an effective method to improve catalytic activity. Xia's team reported that adjusting $MoS_2$ energy level by doping the transition metal can improve HER performance [98]. The Mo 3d of Zn-$MoS_2$ shifts towards lower binding energy compared with pure $MoS_2$ (Figs. 13(a) and 13(b)). It shows that the electron density of $MoS_2$ increases after the addition of Zn and enhances the HER performance (Figs. 13(c) and 13(d)). The energy levels of Zn-$MoS_2$, Fe-$MoS_2$, and pure $MoS_2$ are 5.55, 6.58, and 6.86 eV, respectively (Fig. 13(e)). In addition to the energy level matching, the electrocatalytic activity is also affected by many other complex factors, such as coordination environment (Fig. 13(f)), the number of active sites, and conductivity. The research indicates that Zn-$MoS_2$ has multiple active sites, high kinetic process, and fast charge transfer rates. The significant increase in the electrical conductivity of Zn-$MoS_2$ accelerates the HER kinetics and improves the utilization efficiency of active sites. Zhou's team reported that $MoS_2$ exhibits higher catalytic activity after 55% Re doping into $MoS_2$, inducing the formation of a stable twisted tetragonal structure [99]. DFT calculation reveals that the basal plane of distorted tetragonal (DT) structure alloy catalyst is active. The most active sites in $Re_{0.55}Mo_{0.45}S_2$ are the enriched Mo atoms located the channels between relatively wide cation chains in DT structure. Due to the strong bond energy between S and metal atoms, the structure remains stable during HER reaction, and the adsorption energy of hydrogen is as low as 0.06 eV. In the $Re_xMo_{1-x}S_2$ 1L alloy, stable DT phase $MoS_2$ can be obtained when the Re concentration exceeds 50%. However, it should be noted that Re atoms are not catalytic active sites and will reduce the catalytic activity. The short Re–S bonds deplete catalytic active states near the Fermi energy. The Re doping only converts the H phase to the stable DT phase. When the Re concentration increases above 55%, the stable DT phase structure can still be produced. However, the proportion of active Mo in the DT-$MoS_2$ structure decreased, resulting in the decreased HER activity. The results show that doping elements in $MoS_2$ can induce a stable DT phase structure, and activate the basal plane.

In order to improve the density and conductivity of active sites, Liu et al. synthesized Pt@$MoS_2$ by doping Pt in $MoS_2$ lattice, realizing partial transformation of $MoS_2$ from 2H phase to 1T phase [100]. Pt doping locates in the Mo vacancy of 1T-$MoS_2$, which obviously enhances the catalytic activity. The absolute value of $\Delta G_H$ of Pt@$MoS_2$ is the smallest compared with other different active sites. It indicates that HER reaction occurs at the S-site close to the Pt atom. The density of state (DOS) of different S atoms was analyzed to prove the electronic structures, elucidating the contribution of Pt atoms. The DOS results reveal that the pristine $MoS_2$ has more filled p-states than Pt@$MoS_2$, indicating that the interaction with hydrogen is weakened. This may be due to the ionization energy of Pt is larger than Mo, and the electron density of S atoms near Pt is smaller than original S atoms near the Mo. Experimental and DFT results reveal that Pt doping into $MoS_2$ greatly activates the pristine $MoS_2$ by potential cycling and realizes the phase transition from 2H to 1T.

#### 4.1.3 *Co doping*

Chemical doping can effectively adjust the electronic structure of $MoS_2$ and the adsorption of hydrogen or oxygen-containing radical. At present, theoretical research and numerous experiments reveal that $MoS_2$ doping with metals and heteroatoms such as Ni, Co, W, Se, N, and P can effectively modulate the electronic structure of relevant active sites and exhibit excellent water splitting performance. Su et al. optimized the electronic state of $MoS_2$ by employing N and Mn to obtain a highly active catalytic centers and accelerate the HER kinetics (Figs. 14(a) and 14(b)) [101]. For the pristine $MoS_2$, the Mo-edge site presents the smaller $|\Delta G_{H^*}|$ than the S-edge site and the basal

**Table 2** The HER and OER performances of element doped $MoS_2$ electrocatalysts

| Catalysts | Electrolyte | | $\eta_{10(HER)}$ (mV) | $\eta_{10(OER)}$ (mV) | Tafel$_{(HER)}$ (mV·dec$^{-1}$) | Tafel$_{(OER)}$ (mV·dec$^{-1}$) | Stability | Reference |
|---|---|---|---|---|---|---|---|---|
| | HER | OER | | | | | | |
| C-$MoS_2$ | 1.0 M KOH | — | 45 | — | 46 | — | Chronoamperometric curve recorded at −0.1 V for 240 h | [102] |
| NP-$MoS_2$ | 1.0 M KOH | — | 78 | — | 51,6 | — | 500 mA·cm$^{-2}$ for 20 h | [103] |
| Zn/$MoS_2$ | 0.5 M $H_2SO_4$ | — | 194 | — | 78 | — | Polarization curves for 1,000 cycles | [104] |
| Ag-$MoS_2$ | — | 1.0 M KOH | — | 370 | — | 58.6 | 1.55 V for 22 h | [53] |
| Zn-$MoS_2$ | 0.5 M $H_2SO_4$ | — | 130 | — | 51 | — | Polarization curves for 1,000 cycles | [98] |
| Co-BDC/$MoS_2$ | 1.0 M KOH | — | 155 | — | 86 | — | Polarization curves for 2,000 cycles | [34] |
| mPF-Co-$MoS_2$ | 0.5 M $H_2SO_4$ | — | 156 | — | 74 | — | Polarization curves for 5,000 cycles | [105] |
| Pd, Ru-$MoS_{2-x}OH_y$ | 1.0 M KOH | — | 45 | — | 45 | — | Chronoamperometry at 10 mA·cm$^{-2}$ for 100 h | [106] |
| Rh-$MoS_2$ | 0.5 M $H_2SO_4$ | — | 47 | — | 24 | — | Polarization curves for 2,000 cycles | [107] |
| P-$MoS_2$ | 0.5 M $H_2SO_4$ | — | 43 | — | 34 | — | 100 mV for 20 h | [93] |
| (N,$PO_4^{3-}$)-$MoS_2$/VG | 0.5 M $H_2SO_4$ | — | 85 | — | 42 | — | 10 mA·cm$^{-2}$ for 10 h | [95] |
| Pd-$MoS_2$/CP | 0.5 M $H_2SO_4$ | — | 78 | — | 62 | — | Polarization curves for 5,000 cycles | [97] |
| $Re_{0.55}Mo_{0.45}S_2$ | 0.5 M $H_2SO_4$ | — | 169 | — | 56 | — | Polarization curves for 3,000 cycles | [99] |
| Pt@$MoS_2$ | 0.5 M $H_2SO_4$ | — | 88.43 | — | 55.69 | — | −0.13 V for 20 h | [100] |
| N, Mn-$MoS_2$ | 1.0 M KOH | — | 66 | — | 50 | — | 150 mV for 50 h | [101] |
| Co/Se-$MoS_2$-NF | 0.5 M $H_2SO_4$ | — | 104 | — | 67 | — | 1000 mV for 360 h | [52] |

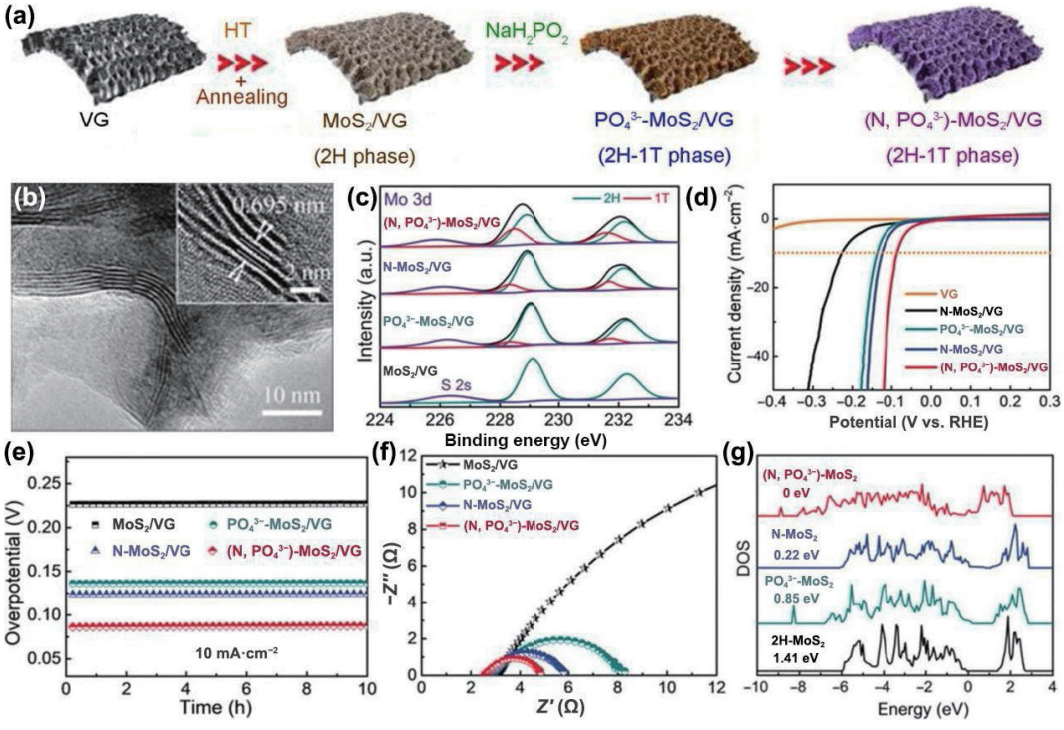


**Figure 12** (a) Schematic fabrication processes. (b) HRTEM images. (c) Mo 3d spectra. (d) Polarization curves. (e) Electrochemical stability. (f) EIS. (g) DOS plots of 2H-$MoS_2$, $PO_4^{3-}$-$MoS_2$, N-$MoS_2$, and (N, $PO_4^{3-}$)-$MoS_2$. Reproduced with permission from Ref. [95], © Wiley-VCH Verlag GmbH & Co. KGaA, Weinheim 2019.

plane, indicating that Mo-edge site is more favorable to HER. Compared with Mo-edge sites of the pristine $MoS_2$, the $\Delta G_{H^*}$ of Mn-$MoS_2$ becomes negative, indicating stronger H* adsorption. However, the $\Delta G_{H^*}$ of S-edge sites obviously reduces after Mn doping, indicating that the adsorption of H* at S-edge sites is weaker. The results show that Mn doping can significantly improve the intrinsic activity of S-edge sites. When Mn and N are co-doped, Mn-N-Mo and Mo-N-Mo exist in N, Mn-$MoS_2$. In addition, Mn and N doping mainly change the HER activity of the S-edge sites, Mo-edge sites, and basal plane (Figs. 14(c)–14(e)). The result of electron differential density reveals that Mn and N doping can effectively improve conductivity of $MoS_2$, optimize electronic structure of active site, and promote the adsorption and desorption of H*, resulting in enhanced HER performance (Figs. 14(f) and 14(g)).

Many researchers reported that the catalytic active sites of

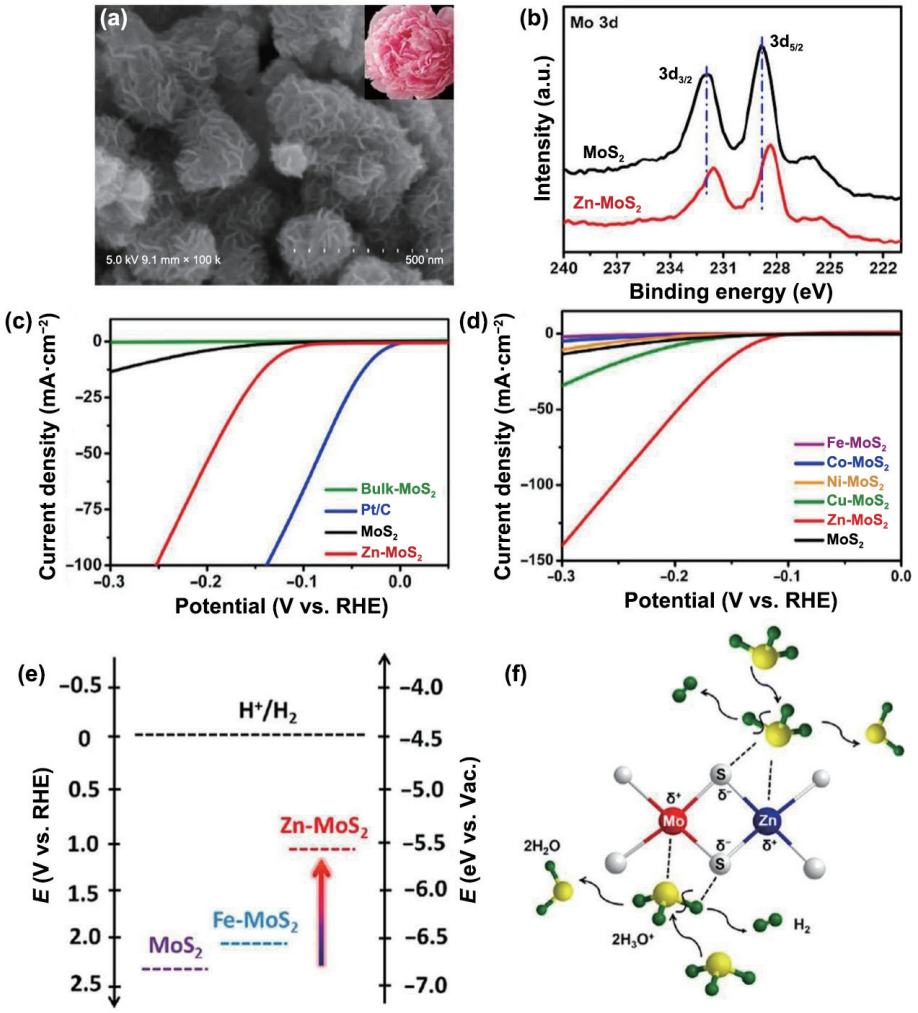


**Figure 13** (a) FESEM image of Zn-$MoS_2$. (b) Mo 3d spectra. (c) and (d) Polarization curves. (e) Band structure diagram for Zn-$MoS_2$, Fe-$MoS_2$, and pure $MoS_2$. (f) Schematic illustration of formation of undercoordinated Mo ($\delta^+$) and Zn ($\delta^+$) centers during the HER and the plausible reaction mechanism. Reproduced with permission from Ref. [98], © American Chemical Society 2017.

intrinsic $MoS_2$ are mainly marginal S sites, and most of S sites on the basal plane are inert and cannot be effectively utilized. Doping metals and heteroatoms into $MoS_2$ lattice can effectively activate S atoms and improve catalytic activity of basal plane. However, it inevitably leads to the hyperactivation of the edges and strong interaction with H*, which is detrimental to HER activity. Therefore, it is necessary to selectively activate inert basal plane and stabilize edge sites to enhance the activity of $MoS_2$. Deng's group synthesized metal and heteroatom co-doping $MoS_2$ electrocatalysts by limiting Se on the surface and Co in the inner layer to activate inert basal plane and stabilize the edges [52]. The H* adsorption at the basal plane S sites is significantly enhanced through co-doping. However, the H* adsorption at the Mo-edge S sites is inevitably excessive, which is adverse for HER. The Se atoms can reduce the excessive adsorption of H* on the co-doping basal plane and Mo-edge sites and result in superior HER activity. These results reveal a synergistic effect between the activation effect of inner Co doping and the stabilization effect of surface Se doping in Co/Se co-doping $MoS_2$.

## 4.2 Vacancy fabrication

Theoretical calculations and experimental results reveal that the introduction of S vacancy in the inert basal plane can expose more edge sites and increase the disorder. Zhang's team reported the optimization and activation of the basal plane of 1L 2H-$MoS_2$ by introducing S vacancy and stress [108]. The $MoS_2$ is exposed to mild Ar plasma to remove part of S (Fig. 15(a)). The theoretical and experimental results indicate that the S vacancies are effective catalytic active sites in the basal plane (Figs. 15(b)–15(d)). The gap state near the Fermi level, created by S vacancies and elastic strain, can enable the exposed Mo atoms to directly bond with hydrogen atoms. Surface S vacancies can adjust the $\Delta G_H$ to modulate the catalytic activity. With the proper combination of S vacancies and strains, the best $\Delta G_H$ (0 eV) can be obtained, and the prepared electrocatalysts exhibit the highest intrinsic activity. Combining S vacancies with elastic strain is an efficient strategy to enhance the catalytic activity of $MoS_2$.

Afterward, Chhowalla et al. reported a 2D $MoS_2$ nanosheet with single vacancy. They used He ion microscopy (HIM) and varied the amount of He ions to remove S atoms one by one, resulting in the controllable generation of S vacancies without external damage to the catalyst [109]. Interestingly, the catalytic activity does not increase with the increase of vacancy concentration. Local strain can be found by observing the atomic structure near the vacancy. When the vacancy concentration reaches $5.7 \times 10^{14}$ $cm^{-2}$, it can be observed that the atomic planes of 1L $MoS_2$ are greatly deviated from the equilibrium positions. Especially in the vicinity of vacancy, the interatomic Mo–Mo distance deviates ± 10 pm. The 3% strain and S vacancy can increase the DOS at the Fermi level and promote the electrons transfer. At present, more and more researches indicate that vacancy can effectively improve the catalytic performance. Therefore, various defects engineering strategies such as exfoliation, plasma bombardment, anion doping, template synthesis, and chemical etching have been widely used in

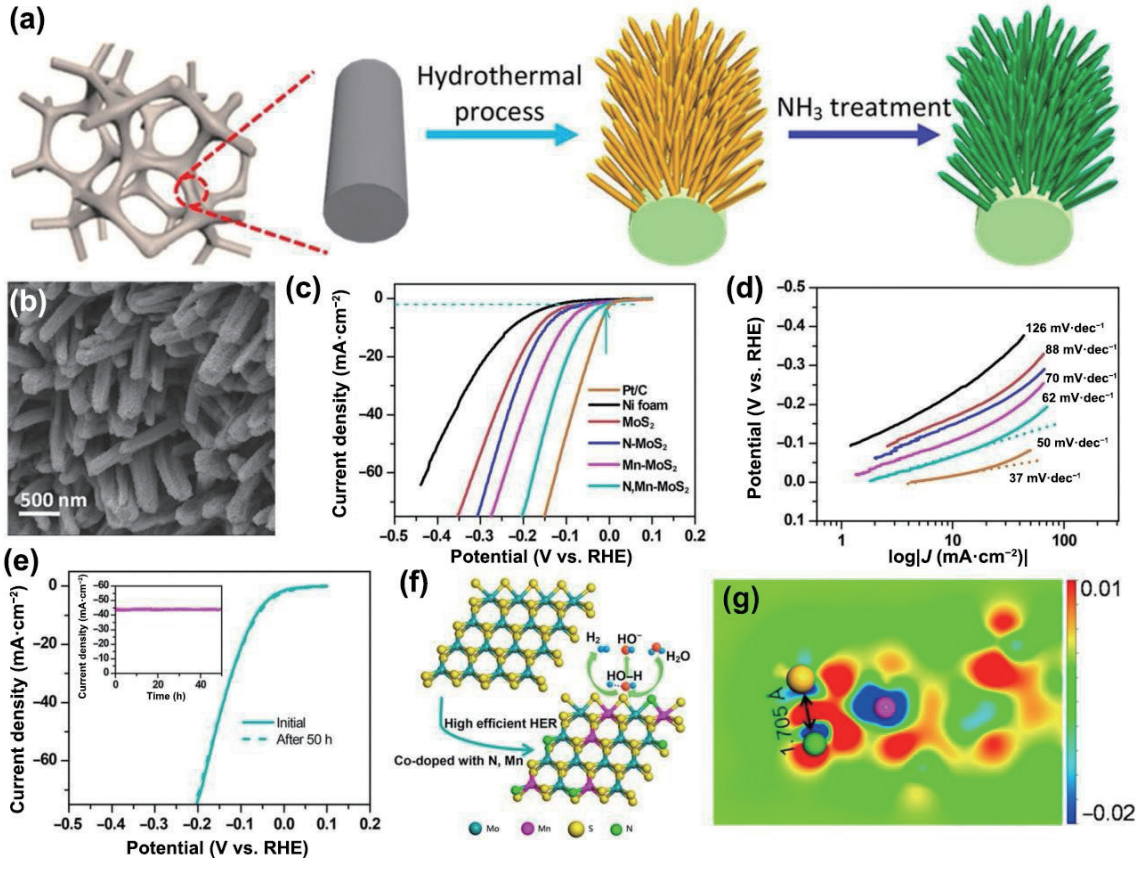


**Figure 14** (a) Schematic illustration of the preparation of N and Mn codoped $MoS_2$. (b) FESEM image. (c) Polarization curves. (d) Tafel slopes. (e) LSV curves of N, Mn-$MoS_2$ before and after 50 h test in 1.0 M KOH. The current density as a function of time at a static overpotential of 150 mV is shown in the inset. (f) Schematic illustration of catalytic HER sites for $MoS_2$ and N, Mn-$MoS_2$. (g) The differential electron density of N, Mn-$MoS_2$. Reproduced with permission from Ref. [101], © American Chemical Society 2018.

the field of electrocatalysis. Zhang's team reported a simple and mild $H_2O_2$ chemical etching method to introduce uniformly distributed single S vacancy on the surface of $MoS_2$ nanosheets [110]. Furthermore, the concentration of S vacancies can be accurately adjusted by systematically changing etching solution concentration, etching time, and etching temperature and as the etching time increases, the lattice spacing of $MoS_2$ also increases (Figs. 15(e)–15(g)). The HER performance of $MoS_2$ is closely related to the concentration and distribution of S vacancies through DFT calculation and experiment. The HER results indicate that the overpotentials and Tafel slopes show the same trends with the increase of etching time (Fig. 15(h)). When the etching time reaches 60 s, the performance of HER is best. EIS and double-layer capacitance ($C_{dl}$) indicate that the appropriate concentration of single S vacancy can significantly promote charge transfer and reduce ohmic loss. The single S vacancy also greatly expands the electrocatalytic active area and forms more catalytic active sites. The electronic structure of electrocatalyst surface is adjusted by the simple and accurate S vacancy tailoring strategy (Fig. 15(i)). The synergistic effect of vacancy concentration and distribution on catalytic performance broadens the field of vacancy design and can be further extended to other types of electrocatalysts and electrocatalytic reactions.

### 4.3 Heterostructure construction

Although $MoS_2$ has been proven to be a superior substitute for noble metal electrocatalysts, the inert basal plane of $MoS_2$ limits the catalytic activity. The intrinsic conductivity of $MoS_2$ is poor, resulting in a large $R_{ct}$ and hindering electrocatalytic reaction. The $MoS_2$ heterostructure construction has been proved to be an effective strategy to improve the catalytic performance of $MoS_2$-based catalysts (Table 3). Moreover, the synergy between two components would lead to the rearrangement of charges at the interface, which is beneficial to the adsorption and desorption of H* and O intermediates in water splitting process. Qu's team prepared the in-plane heterostructure electrocatalysts through coupling the $MoS_2$ (002) basal plane with α-MoC (111) plane [111]. Due to the mismatch of lattice parameters between $MoS_2$ and α-MoC, compressive strain is introduced into the $MoS_2$ basal plane, which can regulate the electronic structure of $MoS_2$. This resulted in the optimal catalytic sites on the $MoS_2$ basal plane change from edge S atoms to edge Mo atoms. DFT results indicate that the favorable active site for HER in acidic solution is the Mo atom. The tensile strain of the basal plane expands interlayer spacing of $MoS_2$ and exposes more edge sites of $MoS_2$. The increased interlayer spacing of $MoS_2$ provides multiple mass transfer pathways for proton migration, adsorption, binding, and hydrogen molecule release, which further promotes the kinetics. As a favorable coupling material, α-MoC can change the electronic structure of $MoS_2$, improve the electrical conductivity of the in-plane $MoS_2$/α-MoC heterostructure, and promote the formation of HER active sites in acidic solution. Furthermore, in alkaline and neutral media, the water splitting activity is enhanced, maximizing the catalytic activity of the active sites. Wu et al. prepared the $MoS_2/Fe_5Ni_4S_8$/FeNi heterojunction with strong coupling interface (Figs. 16(a)–16(c)) [112]. DFT results reveal that the edge S sites of FeNi doped $MoS_2$ are easier to adsorb H than those of $MoS_2$ surface. Therefore, it would be inferred that $MoS_2/Fe_5Ni_4S_8$ coupling interface can promote –OH absorption to improve the OER performance. The lower chemisorption enables the H atoms to be more easily adsorbed on the S sites of the electrocatalysts interface, which in turn reduces the $\Delta G$ of the

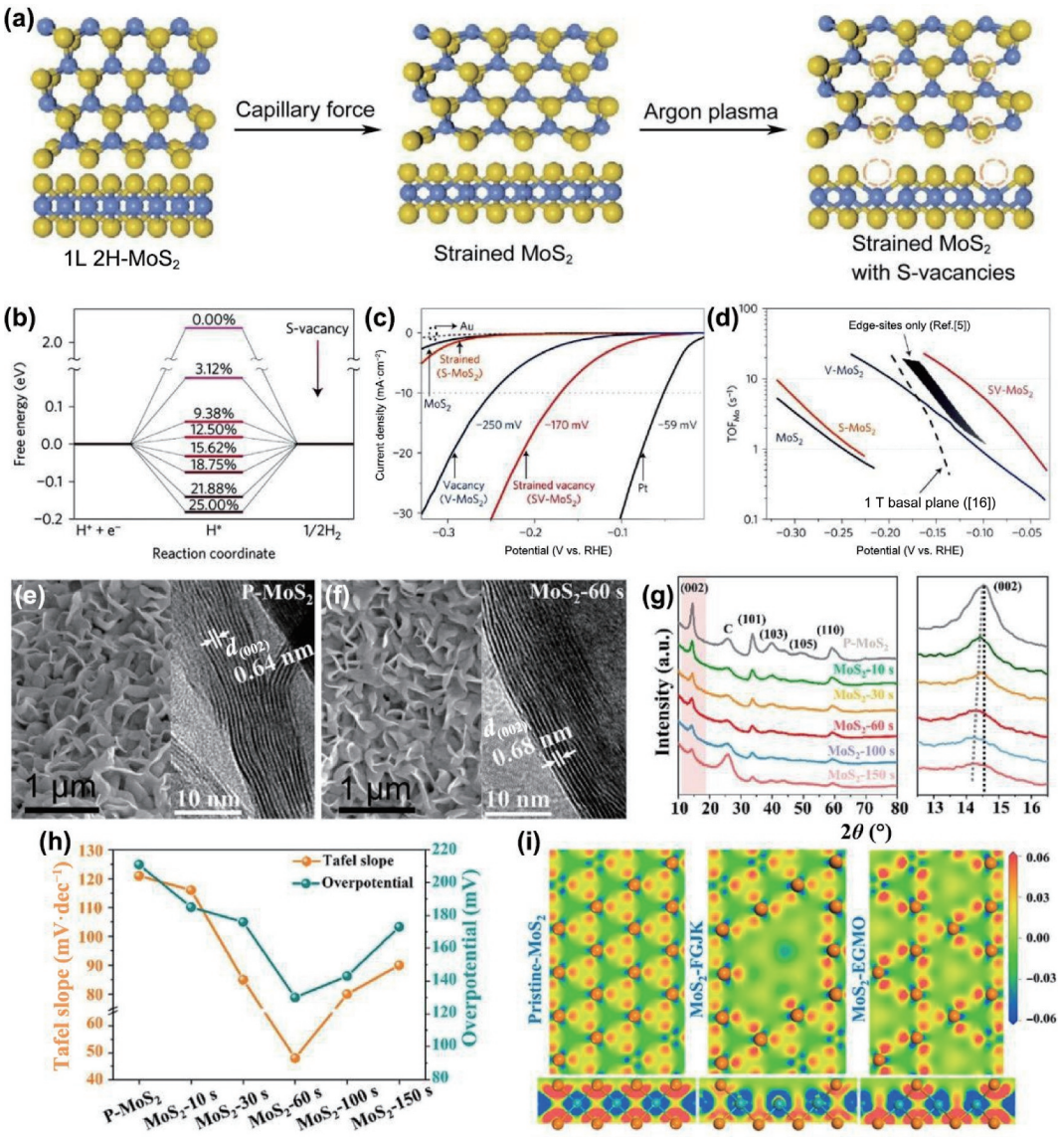


**Figure 15** (a) Schematic of the top (top panel) and side (lower panel) views of pristine 1L 2H-$MoS_2$. (b) Free energy versus the reaction coordinates of HER for the S-vacancy range of 0%–25%. (c) Polarization curves. (d) Turnover frequency per surface Mo atom ($TOF_{Mo}$) of various $MoS_2$ samples. Reproduced with permission from Ref. [108], © Macmillan Publishers Limited 2016. (e) and (f) FESEM and HRTEM images. (g) XRD patterns. (h) Tafel slope and overpotential. (i) Top-view and side view electron density difference maps. Reproduced with permission from Ref. [110], © American Chemical Society 2020.

corresponding intermediates (Figs. 16(d)–16(f)). In addition, the coupled interface of $MoS_2/Fe_5Ni_4S_8$ is favorable for the adsorption of intermediates, reducing the $\Delta G$ of oxygen-containing intermediates and promoting the OER performance (Fig. 16(g)).

The electrical conductivity and catalytic activity of $MoS_2$-based catalysts can be enhanced by surface defect engineering and constructing heterostructures. The oxide surface has strong chemical adsorption for –OH and O-containing intermediates to promote water oxidation process. Therefore, the rational design of heterostructures has great advantages for realizing the synergy between $MoS_2$ and oxides and improving the adsorption of H and O-containing intermediates. Kim's group utilized $Co_3O_4$ and $MoS_2$ to construct heterostructure to promote water splitting process [113]. An efficient heterointerface is formed due to the strong electrostatic interaction between the positively charged $Co_3O_4$ and negatively charged $MoS_2$. The interface between $Co_3O_4$ and $MoS_2$ exposes more active sites facilitating the chemisorption of H and –OH intermediates on the interface. In addition, layered $MoS_2$ can provide fast ion transport and shorten the diffusion path, promoting the reaction kinetics. Yu et al. assembled vertical graphene nanosheets, $MoS_2$ nanosheets, and layered FeCoNi hydroxide on carbon fibers to prepare multilayer stacked heterostructure [114]. The rate-determining step of $MoS_2/FeCoNi(OH)_x$ is changed due to charge redistribution. Fe ions on $MoS_2/FeCoNi(OH)_x$ play a crucial role in OER process as effective active sites, indicating that unsaturated coordinating Fe ions promote OER reaction. DOS shows that $MoS_2/FeCoNi(OH)_x$ has an almost negligible band gap, which is favorable for charge transfer. The charge differential density reveals electron transfer from $FeCoNi(OH)_x$ to $MoS_2$ leading to the accumulation of holes on $FeCoNi(OH)_x$ and promoting the adsorption and dissociation of O-containing intermediates. The binding energy of $MoS_2/FeCoNi(OH)_x$ to the OER intermediate is smaller than single component, which is beneficial to the desorption of the product. The experimental and DFT results show that the recombination of $FeCoNi(OH)_x$ and $MoS_2$ redistributes charge, reduces the OER overpotential, and improves the electrocatalytic activity.

### 4.4 Single atom anchor

Single atom catalysts (SACs) are considered as ideal electrocatalysts owing to the nearly 100% atomic utilization efficiency, and uniform and specific active centers [127–129]. 2D layered $MoS_2$ nanosheets have unique structure and electronic

**Table 3** The HER/OER performances of $MoS_2$-based heterostructures

| Catalysts | Electrolyte | | $\eta_{10(HER)}$ (mV) | $\eta_{10(OER)}$ (mV) | Tafel$_{(HER)}$ (mV·dec$^{-1}$) | Tafel$_{(OER)}$ (mV·dec$^{-1}$) | Stability | Reference |
|---|---|---|---|---|---|---|---|---|
| | HER | OER | | | | | | |
| $Mo_2CT_x$/2H-$MoS_2$ | 0.5 M $H_2SO_4$ | — | 119 | — | 60 | — | Polarization curves for 10 days | [115] |
| $Ni_2P/MoS_2$/N:RGO | 0.5 M $H_2SO_4$ | — | 93.9 | — | 39.5 | — | 150 mV for 60 h | [116] |
| 2.5H-PHNCMs | 1.0 M KOH | 1.0 M KOH | 70 | 235 | 38.1 | 45.7 | −0.31 V and 1.53 V for 24 h | [117] |
| $MoS_2$/FNS/FeNi | 1.0 M KOH | 1.0 M KOH | 120 | 204 | 45.1 | 28.1 | 122 mV and 204 mV for 10 h | [112] |
| $MoS_2$/NiS NCs | 1.0 M KOH | 1.0 M KOH | 92 | 271 ($\eta_{15}$) | 113 | 53 | 10 mA·cm$^{-2}$ for 80 h | [118] |
| $MoS_2/Ni_2V_3O_8$ | 0.5 M $H_2SO_4$ | — | 58 | — | 54 | — | 10, 50, and 100 mA·cm$^{-2}$ for 30 h | [119] |
| CF/VGSs/$MoS_2$/FeCoNi(OH)$_x$ | 1.0 M KOH | 1.0 M KOH | 43 | 225 ($\eta_{500}$) | 25.2 | 29.2 | Overpotential of specific current for 95 h | [114] |
| $NiS_2$-$MoS_2$/PVEIB/PPy/GO | 0.5 M $H_2SO_4$ | — | 45 | — | 49 | — | −0.21 V for 20 h | [120] |
| $NiS_2/MoS_2$ HNW | 1.0 M KOH | — | 204 | — | 65 | — | 10 and 30 mA·cm$^{-2}$ for 6 h | [54] |
| $MoS_2$/NiCoS | 1.0 M KOH | 1.0 M KOH | 189 | 290 | 75 | 77 | 20 mA·cm$^{-2}$ for 20 h | [121] |
| $MoS_2$ QDs@$Mo_2C$@NF | — | 1.0 M KOH | — | 110 | — | 57 | Polarization curves for 5,000 cycles | [122] |
| $MoS_2$/N-RGO-180 | 0.5 M $H_2SO_4$ | — | 56 | — | 41.3 | — | Polarization curves for 5,000 cycles | [123] |
| $MoS_x$@NiO | 1.0 M KOH | — | 406 | — | 43 | — | Polarization curves for 13 h | [124] |
| 1T-$MoS_2/Ni^{2+\delta}O_\delta(OH)_{2-\delta}$ | 1.0 M KOH | — | 73 | — | 77 | — | 10 mA·cm$^{-2}$ for 30 h | [125] |
| Ni@NC@$MoS_2$ | 0.5 M $H_2SO_4$ | — | 82 | — | 47.5 | — | 94 mV for 8 h | [30] |
| CoNC@$MoS_2$ | 1.0 M KOH | 1.0 M KOH | 143 | 350 | 68 | 51.9 | Polarization curves for 1,500 cycles | [126] |
| $Ni_3S_2$@$MoS_2$/FeOOH | 1.0 M KOH | 1.0 M KOH | 95 | 234 | 85 | 49 | 10 mA·cm$^{-2}$ for 50 h | [64] |
| Co, Nb-$MoS_2/TiO_2$ HSs | 1.0 M KOH | 1.0 M KOH | 58.8 | 260 | 40.2 | 65.0 | Polarization curves for 30 h | [37] |
| $Co_3O_4/MoS_2$ | 1.0 M KOH | — | 205 | 230 | 98 | 45 | 1.53 V for 13 h | [113] |
| $MoS_2$/α-MoC | 0.5 M $H_2SO_4$. | — | 78 | — | 38.7 | — | Long-term stabilities for 12 h | [111] |

properties owing to unsaturated coordination S atoms at the edges. At present, there are many anchoring methods for metal single atom on $MoS_2$, including vacancy anchoring, basal plane S atom anchoring, and substitution of Mo atoms. The single atoms can activate the basal plane S atoms and adjust the charge distribution of coordination atoms to promote the catalytic reaction.

Tan's team utilized Ru single atom to replace the Mo atom of $MoS_2$, and explored the relationship between Ru site and S vacancies at alkaline conditions [130]. The synergistic effect between Ru site and S vacancies is amplified through strain engineering. The bending strain effectively regulates the electronic structure of Ru single atom and enhances the accumulation of –OH and $H_2O$ in S vacancies, which results in increased reactant density in the basal plane. The synergistic effect of single atom catalytic sites and defect can promote the catalytic reaction. Li's group optimized the concentration of Ru single atoms and S vacancies to improve the HER performance of 2H-$MoS_2$ [131]. The Ru atoms are embedded in the 2H-$MoS_2$ basal plane by replacing the Mo atoms and coordinating with S atoms. The introduction of Ru single atoms and S vacancies into 2H-$MoS_2$ can enhance the electronic states of S 2p and Ru, conduce to charge transfer, and improve the HER kinetics process. The formation of Ru single atoms and S vacancies leads to differences in the band structures. Compared with other S vacancy concentrations, the optimal $MoS_2$ electrocatalysts reveal the smallest band gap. The increased DOS near Fermi level can accelerate charge transfer kinetics and improve HER performance. Ru single atoms can activate the S atoms close to Ru, and the interaction with Mo atoms around S vacancies is enhanced to affect the H adsorption. Xu et al. synthesized porous 1T-$MoS_2$ with S vacancy and Cu single atom by simple one-step solvothermal synthesis [132]. For 1T-$MoS_2$ with porous structure, Cu single atoms can activate basal plane and provide more active edge sites. The Cu single atoms can accelerate the electron transfer from Cu to $MoS_2$ and increase the electron density on the surface of $MoS_2$. More importantly, the DFT calculation reveals that Cu single atoms anchored on 1T-$MoS_2$ surface are more stable and the charge transfer is faster than that anchored on 2H-$MoS_2$ surface. Therefore, metastable 1T-$MoS_2$ has potential advantages over 2H-$MoS_2$ in anchoring single metal atom, which is helpful to improve the performance of HER.

Deng's group constrained the distance of Rh single atoms in $MoS_2$ lattices to enhance catalytic activity of $MoS_2$ [133]. DFT calculation indicates the active sites and reaction mechanism of the catalysts. Mo atoms are replaced by Rh on the $MoS_2$ basal plane, which activates the adsorption of H on S atoms near Rh. The localized electronic structure of neighboring S atoms is modulated by restricting Rh atoms in the $MoS_2$ lattice. The DOS of neighboring S atoms near the Fermi level can be increased, reflecting the trend of HER activity with Rh distance. The experimental results show that Rh single atoms in the $MoS_2$ lattice can adjust the electronic structure of adjacent S atoms and optimize the adsorption energy of H at the S sites. With the

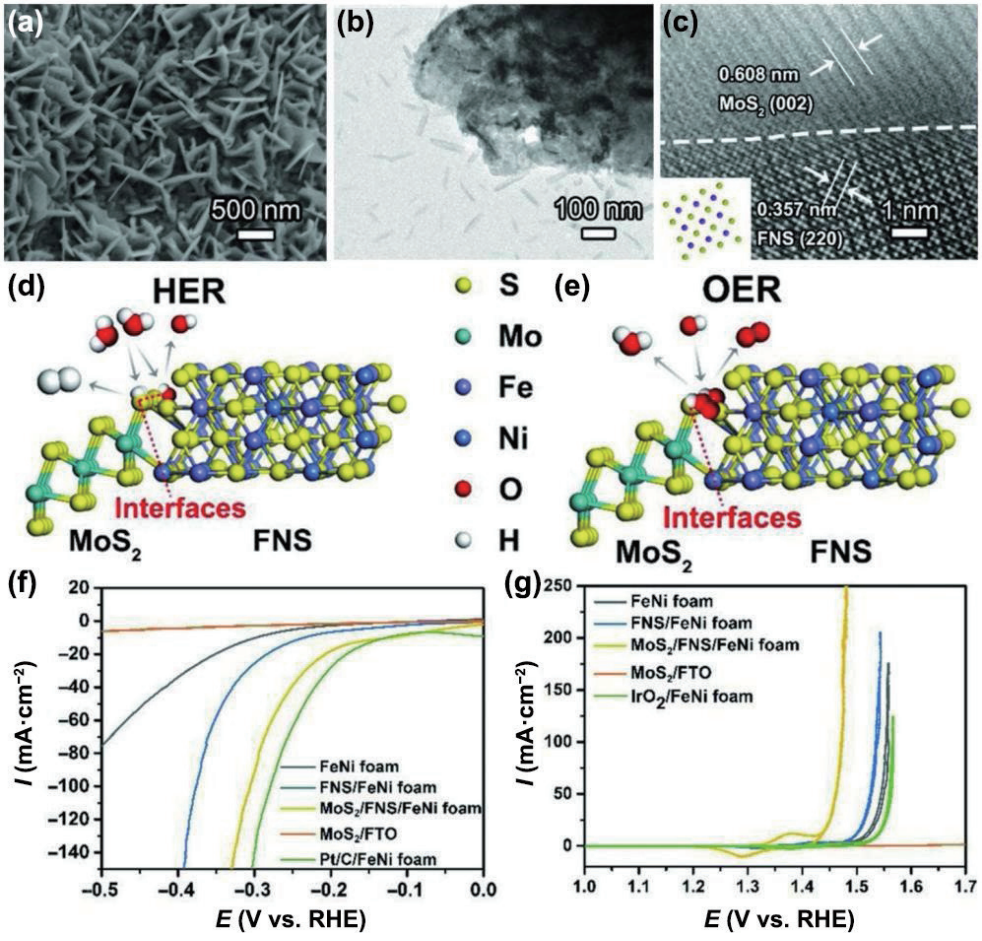


**Figure 16** (a) FESEM image. (b) and (c) TEM and HRTEM images. (d) and (e) The mechanisms of $MoS_2$/FNS coupling interfaces acting on HER and OER. (f) Polarization curves. (g) CV curves. Reproduced with permission from Ref. [112], © WILEY-VCH Verlag GmbH & Co. KGaA, Weinheim 2018.

reduction of the Rh atomic spacing, the H adsorption free energy of the adjacent S sites on the basal plane exhibits a volcano-type trend. When the distance between Rh atoms is optimal, the electronic state strength and energy level are decreased, and the adsorption of H is weakened.

The coordination of one metal atom with four nitrogen atoms ($M\text{-}N_4$) is generally considered as the active center for various electrocatalytic reactions [134]. Compared with ordinary $M\text{-}N_4$ sites, other sites can adjust the catalytic activity of single atom catalysts by modulating the electronic states of metal atoms. Liu et al. hybridized the Co nanodisks and $MoS_2$ nanosheets (Fig. 17(a)) to combine the Co single atoms array with 1T-$MoS_2$ nanosheets through covalent combination of Co and S atoms (Figs. 17(b)–17(d)). The strain caused by the formation of Co–S covalent bonds between Co and $MoS_2$ leads to the phase transition of $MoS_2$ [60]. The transformation of 2H-$MoS_2$ to 1T-$MoS_2$ is induced by coordination reconfiguration of Co atoms, in which Co single atom is the main catalytic center. Co is transformed from cationic to metallic due to electron effect or ligand effect and charge density wave state transition. In this case, the increase in the empty state of Co atoms near the Fermi level suggests that it can promote the hybridization between Co atoms and H atoms. This is considered that it can promote HER activity in thermodynamics process. DFT calculation confirms that the high HER activity of the single atom catalysts (Figs. 17(e) and 17(f)) is mainly due to the ensemble effect of Co adsorbed atoms and S, which adjusts the hydrogen binding mode at the interface (Fig. 17(g)). The Co atoms are coordinated with three adjacent S atoms and located directly above the center of Mo atoms, promoting the catalytic reaction.

## 5 Breakthroughs on $MoS_2$ electrocatalysts for overall water splitting

The development of low-cost and high-efficiency bifunctional water electrolysis catalysts is an important way to improve the overall water splitting efficiency. However, the electrocatalytic activity of $MoS_2$ for overall water splitting is limited due to the high overpotential and slow kinetic process of OER. The pH of the electrolyte limits the overall water splitting activity due to pH-dependence. Adjusting the electrode/electrolyte interface can prevent sulfide oxidation and S leaching at the interface, enrich active centers, and promote electron transfer. At present, most studies focus on enhancing the HER or OER electrocatalytic activity of $MoS_2$, while ignoring the development of bifunctional electrocatalysts with high HER and OER activity at the same time. Integrating HER and OER electrocatalysts into a single nanostructure has become one of the hottest issues in the field, which holds promise for efficient overall water splitting (Table 4).

It is more favorable for OER progress in alkaline electrolyte and the HER in acidic electrolyte. Therefore, it is very important to develop a highly efficient catalyst that can reveal superior HER and OER performance in specific electrolytes and achieve overall water splitting. Zhao et al. reported that Co covalent doping in $MoS_2$ to induce bifunctionality of overall water splitting [136]. The feasibility of conversion from $Mo_2C$ to $MoS_2$ and the optimal proportion of Co covalent doping $MoS_2$ were confirmed via DFT calculation. Through the optimization model, it is further proved that Co covalent doping $MoS_2$ presents metallic characteristics and band gap is 0 eV, indicating the Co covalent doping $MoS_2$ would be conducive to promote the catalytic reaction. In 1.0 M KOH electrolyte, the catalyst reveals low HER and OER overpotentials

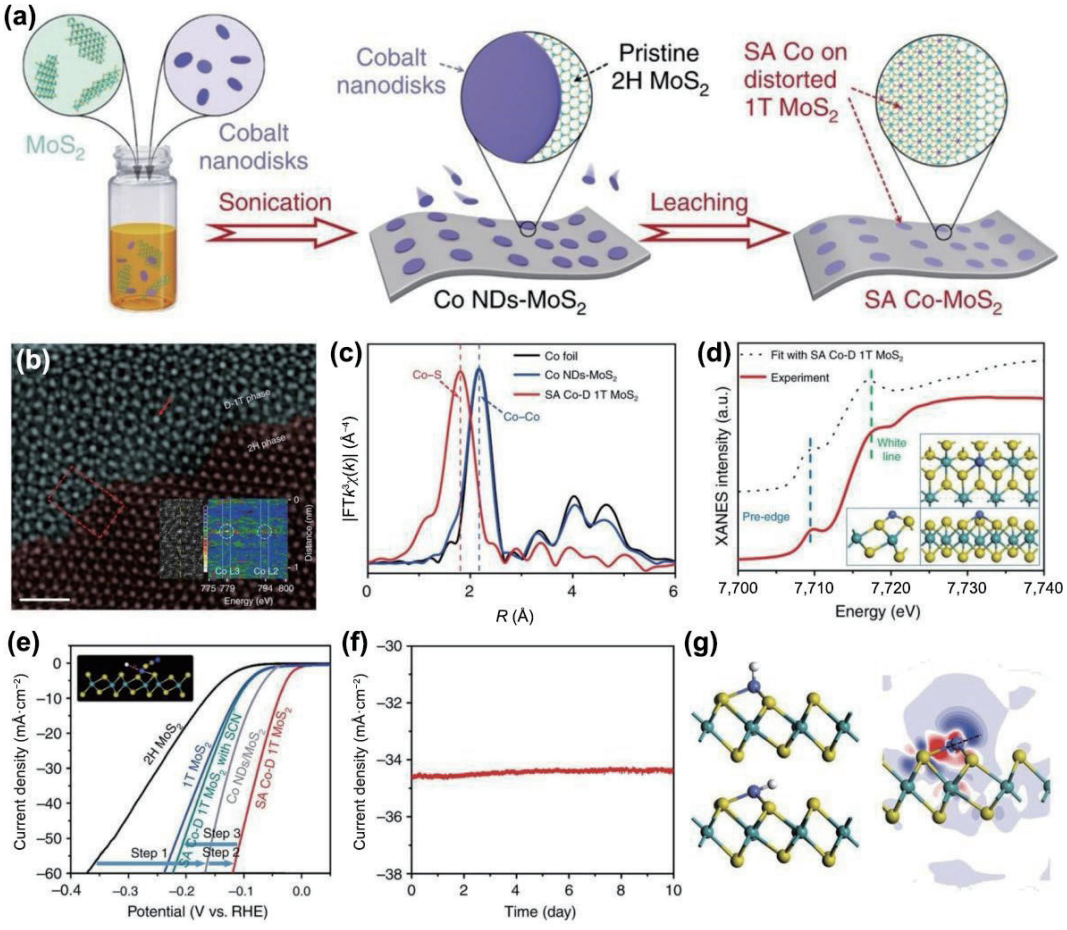


**Figure 17** (a) Schematic illustration of the fabrication process for SA Co-D 1T $MoS_2$. (b) Aberration-corrected HAADF-STEM image of SA Co-D 1T $MoS_2$, showing the obvious junction between SA Co-D 1T $MoS_2$ (dark cyan) and pristine 2H $MoS_2$ (wine). The inset shows the HRTEM and EELS spectrum of SA Co-D 1T $MoS_2$ (scale bar: 1 nm). (c) FT-EXAFS spectra of SA Co-D 1T $MoS_2$ and bulk cobalt foil at the Co K-edge. (d) Co K-edge XANES of SA Co-D 1T $MoS_2$ and fitted curve. The inset shows the atomic structure of SA Co-D 1T $MoS_2$. (e) Polarization curves. (f) Time dependence of the current density for SA Co-D 1T $MoS_2$ at a static overpotential of 100 mV vs. RHE. (g) Hydrogen adsorption modes on the single-atom Co-$MoS_2$ 3 × 3 case and the electron density difference. Reproduced with permission from Ref. [60], © Qi, K. et al. 2019.

of 48 and 260 mV, respectively. The change of the atomic coordination environment of the catalysts is verified through *operando* extended X-ray absorption fine structure (EXAFS) to prove the source of the bifunctional. In HER, K-edge EXAFS spectra of Co and Mo of Co-$MoS_2$/BCCF show no obvious change in the related bonds of Co and Mo after 50 cycles of polarization curve measurements. However, in OER, the EXAFS spectra reveal that after 50 cycles, both Co- and Mo-related bonds changed. The Co–O and Mo–O bonds can be observed in the Co and Mo K-edge of the catalyst after anode circulation, proving that formed $Co^{3+/4+}$ and other high valence Co species at anodic potential in alkaline medium. Compared with $MoS_2$/BCCF, the OER activity of Co-$MoS_2$/BCCF mainly originates from the formation of high-valent Co species in alkaline solution at anodic potential.

Extensive experiments have demonstrated that interfacial reconfiguration of the heterojunction can promote the water splitting process. The electrocatalytic performance is better than that of single-component catalysts, and it can be used as an efficient catalyst for overall water splitting. The $Ni_3S_2$ reveals superior catalytic activity for OER, and $MoS_2$ can effectively promote the HER. Therefore, the $Ni_3S_2$ and $MoS_2$ are combined to construct heterostructures and promote the overall water splitting. Gao et al. prepared $MoS_2$–$Ni_3S_2$ heterostructure with nickel foam as carrier to achieve enhancement of HER, OER, and overall water splitting [137]. In the composite electrocatalysts, $Ni_3S_2$ nanorods are uniformly combined with $MoS_2$ nanosheets to form a superior heterogeneous interface, which is favorable for the chemisorption of H- and O-containing intermediates. The efficient exposure of active interfaces in hierarchical nanostructures promotes of electron transfer the $Ni_3S_2$ on NF substrates. Thus, the catalytic performance of the overall water splitting is improved. Besides the construction of $MoS_2$ heterostructures, transition metal doping is also an effective way to construct bifunctional electrocatalysts for water splitting. It has been developed into a stable and highly active overall water splitting catalyst. Kang's group used Ru nanoparticles to modify Co-doped 1T-$MoS_2$ to obtain an efficient overall water splitting catalyst [138]. The catalysts were prepared by the Co atoms uniformly replacing Mo atoms in 1T-$MoS_2$ and hybridized with Ru nanoparticles. DFT calculation reveals the superior HER activity of CoRu-$MoS_2$ due to superior adsorption and dissociation of water on the (002) plane of Ru. The Co atoms boost the adsorption and dissociation of intermediates and accelerate HER. Due to the modification of Ru nanoparticles, the electronic structure of the catalyst is optimized. The synergistic effect among components and unsaturated coordination environment enable the catalyst to exhibit superior bifunctionality. Hou et al. used oxidation/hydrogenation and induced surface reconstruction to prepare multistage transition bimetallic oxide/sulfide heterostructure arrays, realizing the modulation of geometry and optimization of charge transfer [135]. Transition bimetallic oxide/sulfide heterostructure array as an electrocatalytic material presents industrial application prospect. The superior electrocatalytic performance benefits from the simultaneous modulation of geometry, the systematic optimization of charge

**Table 4** The overall water splitting actives of $MoS_2$-based catalysts

| Catalysts | Electrolyte | | $\eta_{10(HER)}$ (mV) | $\eta_{10(OER)}$ (mV) | Tafel$_{(HER)}$ (mV·dec$^{-1}$) | Tafel$_{(OER)}$ (mV·dec$^{-1}$) | Stability | Reference |
|---|---|---|---|---|---|---|---|---|
| | HER | OER | | | | | | |
| $MoS_2$-$NiS_2$/NGF | 1.0 M KOH | 1.0 M KOH | 172 | 370 | 70 | — | 10 mA·cm$^{-2}$ for 24 h | [139] |
| CoS-$Co(OH)_2$/a$MoS_{2+x}$ | 1.0 M KOH | 1.0 M KOH | 143 | 380 | 68 | 68 | 10 mA·cm$^{-2}$ for 100,000 s | [140] |
| $Co_5Mo_{10}S_x$/CC | 1.0 M KOH | 1.0 M KOH | 36 | 153 | 56 | 58 | Polarization curves for 2,000 cycles | [141] |
| (Ni, Fe)$S_2$@$MoS_2$ | 1.0 M KOH | 1.0 M KOH | 130 | 270 | 101.22 | 43.21 | 10 mA·cm$^{-2}$ for 44 h | [142] |
| Ir/$MoS_2$ | 1.0 M KOH | 1.0 M KOH | 44 | 330 | 32 | 44 | Polarization curves for 9,000 cycles | [143] |
| $MoS_2$-$Ni_3S_2$ | 1.0 M KOH | 1.0 M KOH | 98 | 249 | 61 | 57 | 150 mV for 48 h | [137] |
| NiMoS/NF | 1.0 M KOH | 1.0 M KOH | 78 | 260 | 68 | 59 | –150 and 370 mV for 48 h of HERand OER | [144] |
| CoMoS | 1.0 M KOH | 1.0 M KOH | 97 | 272 | 70 | 45 | 1.6 V for 10 h | [145] |
| Co-$MoS_2$/BCCF | 1.0 M KOH | 1.0 M KOH | 48 | 260 | 52 | 85 | 70 mV for 40,000 s | [136] |
| CoRu-$MoS_2$ | 1.0 M KOH | 1.0 M KOH | 52 | 308 | 55 | 50 | Current from 10 to 20, 40, and back to 10 mA·cm$^{-2}$ for 16 h. | [138] |
| $NiMoO_x$/NiMoS | 1.0 M KOH | 1.0 M KOH | 38 | 186 | 38 | 34 | 500 mA·cm$^{-2}$ at 1.75 V for 500 h | [135] |

transfer, and the constructed heterostructure interface (Fig. 18(a)). In the OER process, the hydroxide and oxyhydroxides formed the real active site. Although hydroxide and oxyhydroxides formed on the surface of $NiMoO_x$/NiMoS array, the morphology of heterostructure did not change. In the overall water splitting process, the double electrodes assembled by $NiMoO_x$/NiMoS can provide large current density and superior stability required by industry at low potential (Figs. 18(b) and 18(d)). DFT calculation shows that the coupling interface between $NiMoO_x$ and NiMoS optimizes the adsorption energy, accelerates the kinetics, and improves the electrocatalytic performance (Fig. 18(c)).

## 6 Conclusion and outlook

As one of the main hydrogen production methods, electrocatalytic water splitting has received extensive attention. In the past decades, significant progress has been made in the design and preparation of non-noble metal-based catalysts, especially $MoS_2$-based electrocatalysts. Understanding the relationship between catalytic activity and structure is of great significance for modulating the morphology and electronic structure of $MoS_2$, and improving the activity of electrocatalytic water splitting. This review focuses on the following viewpoints and outlook.

(1) $MoS_2$ electrocatalysts with 0D, 1D, 2D, and 3D structures have been developed, and significant progress has been made in modulating the morphology. Among them, 3D structures composed of 2D nanosheets such as Janus, hollow, core–shell, and yolk–shell structures can improve the stability of catalysts due to their high mechanical strength, large active specific surface area, and abundant active sites. Both HER and OER reactions are processes of gas release, and structural modulation can accelerate the process of gas release to promote water splitting.

(2) The basal plane of intrinsic $MoS_2$ is usually inert, and the active center mainly originates from the coordinately unsaturated S atoms at the edge. Therefore, it is meaningful to explore strategies that excite the catalytic activity of inert atoms in the $MoS_2$ basal plane. At present, many methods have been used to activate the catalytic sites of the basal plane, among which doping is one of the common methods. The electron density of Mo and S atoms around the dopant is affected, resulting in charge redistribution, which modulates the electrocatalytic activity of atoms in the basal plane and provides more active sites.

(3) The catalyst surface plays a key role in electrocatalytic reactions, and surface defect is also a key factor in the construction of highly active electrocatalysts. Surface defect can expose more incongruent edge sites and optimize the intrinsic activity. The introduction of S vacancy results in that uncoordinated Mo atoms present vacant state, which is favorable for hydrogen adsorption. The synergistic regulation of S vacancy concentration and distribution affect the catalytic activity. In addition, studies have revealed that S vacancy can serve as important active sites for HER.

(4) The heterostructure construction has been proved to be an effective strategy to improve the catalytic performance of $MoS_2$ electrocatalysts. The interfacial engineering and synergy increase the exposed active sites of $MoS_2$ and can lead to charge rearrangement to promote the adsorption and desorption of H* and O intermediates during water splitting process. For example, the conductivity of $MoS_2$ can be enhanced by constructing heterostructure with $MoO_2$, and the synergistic effect of $MoS_2$ and $MoO_2$ can accelerate electron transfer and promote HER catalytic reaction.

(5) Benefiting from the unsaturated coordination configuration, excellent dispersion, and uniform and specific active centers, single atom catalysts can not only achieve 100% atom utilization efficiency, but also exhibit superior catalytic activity and selectivity. Loading metal single atoms on $MoS_2$ is a superior strategy to enhance the catalytic activity of $MoS_2$. At present, there are many methods for anchoring metal single atom catalysts on $MoS_2$, including vacancy anchoring, basal plane S atom anchoring, and atomic substitution. The researches show that single atom anchored on S vacancy reduces band gap of $MoS_2$, and interacts with the surrounding Mo atoms to activate the surrounding S atoms.

(6) The ultimate goal in developing high-performance electrocatalysts is to realize efficient overall water splitting. Integrating HER and OER electrocatalysts into a single nanostructure has become one of the hottest issues in this field, which holds promise for efficient overall water splitting. During the water splitting process, the pH-dependence of catalysts limited the development of overall water splitting. Numerous studies have shown that acidic electrolyte can promote the HER reaction and alkaline electrolyte can enhance the OER reaction. Therefore, the development of all-pH bifunctional electrocatalysts with low pH-dependence is an important step towards efficient overall water splitting.

(7) The strategies including morphology and electronic

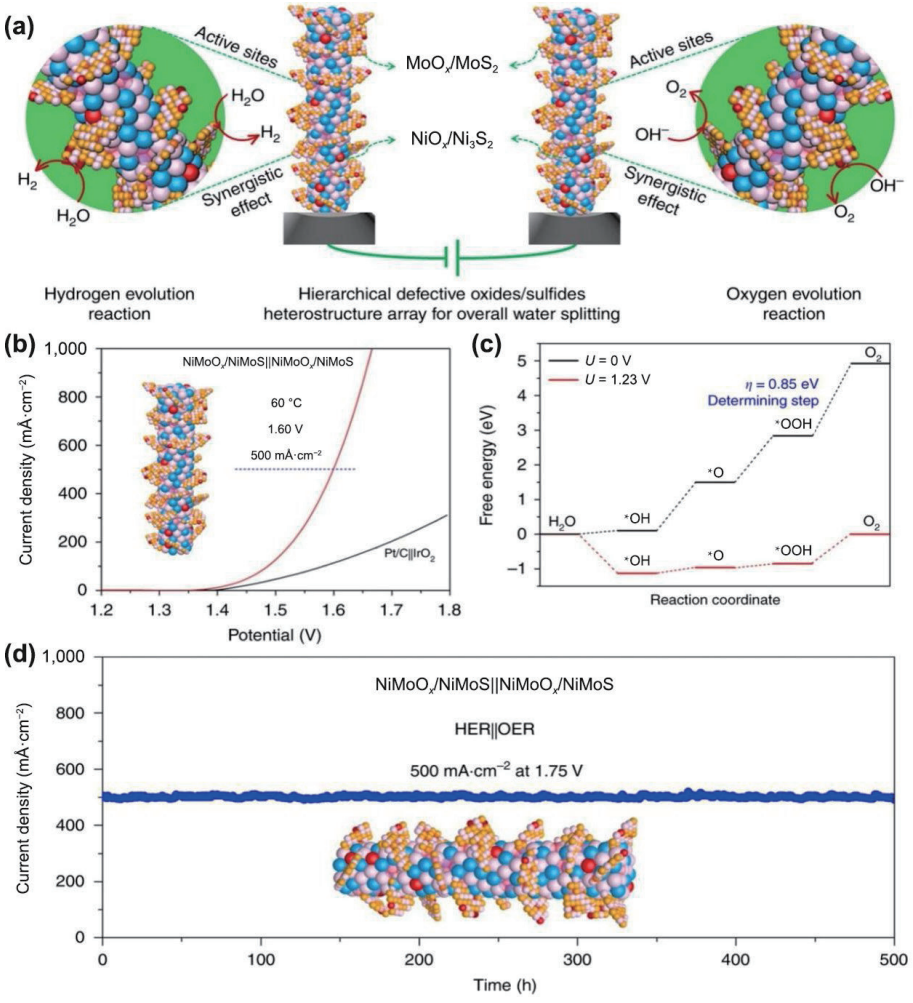


**Figure 18** (a) $NiMoO_x$/NiMoS array as two-electrode-cell towards large-scale electrolysis. Colored balls represent various elements (blue: Mo, pink: S, red: O, and yellow: Ni). (b) Polarization curves by two-electrode system in a 6 M KOH at 60 °C. (c) $NiMoO_x$/NiMoS heterostructures. Cyan, yellow, red, green, and gray balls represent H, S, O, Mo, and Ni atoms, respectively. (d) Chronoamperometric test at 1.75 V in 1.0 M KOH at 25 °C. Reproduced with permission from Ref. [135], © Zhai, P. L. et al. 2020.

structure modulation on $MoS_2$-based catalysts can be further extended to other electrocatalytic reactions, such as $O_2$ reduction, $N_2$ reduction, or $CO_2$ reduction in the future. It should be noted that the OER is the primary reaction for the overall reaction, which provides continuous electrons and protons.

## Acknowledgements

S. Y. designed and supervised the project. All the authors discussed and commented on the manuscript. This work was financially supported by the National Natural Science Foundation of China (No. 21902157), Starting fund for scientific research of high-level talents, Anhui Agricultural University (No. rc382108), the Open Fund of The State Key Laboratory of Catalysis in DICP, CAS (N-21-12), and the Open Fund of The State Key Laboratory of Molecular Reaction Dynamics in DICP, CAS (SKLMRD-K202223).

## References

[1] Zhang, N. Q.; Ye, C. L.; Yan, H.; Li, L. C.; He, H.; Wang, D. S.; Li, Y. D. Single-atom site catalysts for environmental catalysis. *Nano Res.* **2020**, *13*, 3165–3182.

[2] Wang, Q. L.; Xu, C. Q.; Liu, W.; Hung, S. F.; Yang, H. B.; Gao, J. J.; Cai, W. Z.; Chen, H. M.; Li, J.; Liu, B. Coordination engineering of iridium nanocluster bifunctional electrocatalyst for highly efficient and pH-universal overall water splitting. *Nat. Commun.* **2020**, *11*, 4246.

[3] Ye, S.; Shi, W. W.; Liu, Y.; Li, D. F.; Yin, H.; Chi, H. B.; Luo, Y. L.; Ta, N.; Fan, F. T.; Wang, X. L. et al. Unassisted photoelectrochemical cell with multimediator modulation for solar water splitting exceeding 4% solar-to-hydrogen efficiency. *J. Am. Chem. Soc.* **2021**, *143*, 12499–12508.

[4] Yang, J. R.; Li, W. H.; Tan, S. D.; Xu, K. N.; Wang, Y.; Wang, D. S.; Li, Y. D. The electronic metal-support interaction directing the design of single atomic site catalysts: Achieving high efficiency towards hydrogen evolution. *Angew. Chem., Int. Ed.* **2021**, *60*, 19085–19091.

[5] Li, X. P.; Zheng, L. R.; Liu, S. J.; Ouyang, T.; Ye, S. Y.; Liu, Z. Q. Heterostructures of NiFe LDH hierarchically assembled on $MoS_2$ nanosheets as high-efficiency electrocatalysts for overall water splitting. *Chin. Chem. Lett.*, in press, https://doi.org/10.1016/j.cclet.2021.12.095.

[6] Seitz, L. C.; Dickens, C. F.; Nishio, K.; Hikita, Y.; Montoya, J.; Doyle, A.; Kirk, C.; Vojvodic, A.; Hwang, H. Y.; Norskov, J. K. et al. A highly active and stable $IrO_x/SrIrO_3$ catalyst for the oxygen evolution reaction. *Science* **2016**, *353*, 1011–1014.

[7] Wang, Y.; Zheng, M.; Li, Y. R.; Ye, C. L.; Chen, J.; Ye, J. Y.; Zhang, Q. H.; Li, J.; Zhou, Z. Y.; Fu, X. Z. et al. p-d Orbital hybridization induced by a monodispersed ga site on a $Pt_3Mn$ nanocatalyst boosts ethanol electrooxidation. *Angew. Chem., Int. Ed.* **2022**, *61*, e202115735.

[8] Han, A. L.; Wang, X. J.; Tang, K.; Zhang, Z. D.; Ye, C. L.; Kong, K. J.; Hu, H. B.; Zheng, L. R.; Jiang, P.; Zhao, C. X. et al. An adjacent atomic platinum site enables single-atom iron with high

oxygen reduction reaction performance. *Angew. Chem., Int. Ed.* **2021**, *60*, 19262–19271.

[9] Zhang, N. Q.; Zhang, X. X.; Kang, Y. K.; Ye, C. L.; Jin, R.; Yan, H.; Lin, R.; Yang, J. R.; Xu, Q.; Wang, Y. et al. A supported $Pd_2$ dual-atom site catalyst for efficient electrochemical $CO_2$ reduction. *Angew. Chem. , Int. Ed.* **2021**, *60*, 13388–13393.

[10] Jing, H. Y.; Zhu, P.; Zheng, X. B.; Zhang, Z. D.; Wang, D. S.; Li, Y. D. Theory-oriented screening and discovery of advanced energy transformation materials in electrocatalysis. Adv. Powder Mater., in press, https://doi.org/10.1016/j.apmate.2021.10.004.

[11] Cui, C. H.; Gan, L.; Heggen, M.; Rudi, S.; Strasser, P. Compositional segregation in shaped Pt alloy nanoparticles and their structural behaviour during electrocatalysis. *Nat. Mater.* **2013**, *12*, 765–771.

[12] You, B.; Sun, Y. J. Innovative strategies for electrocatalytic water splitting. *Acc. Chem. Res.* **2018**, *51*, 1571–1580.

[13] Guo, D. Z.; Li, X.; Jiao, Y. Q.; Yan, H. J.; Wu, A. P.; Yang, G. C.; Wang, Y.; Tian, C. G.; Fu, H. G. A dual-active Co−CoO heterojunction coupled with $Ti_3C_2$-MXene for highly-performance overall water splitting. *Nano Res.* **2022**, *15*, 238–247.

[14] Gong, M.; Zhou, W.; Kenney, M. J.; Kapusta, R.; Cowley, S.; Wu, Y. P.; Lu, B. G.; Lin, M. C.; Wang, D. Y.; Yang, J. et al. Blending $Cr_2O_3$ into a NiO-Ni electrocatalyst for sustained water splitting. *Angew. Chem., Int. Ed.* **2015**, *54*, 11989–11993.

[15] Dionigi, F.; Zhu, J.; Zeng, Z. H.; Merzdorf, T.; Sarodnik, H.; Gliech, M.; Pan, L. J.; Li, W. X.; Greeley, J.; Strasser, P. Intrinsic electrocatalytic activity for oxygen evolution of crystalline 3d-transition metal layered double hydroxides. *Angew. Chem., Int. Ed.* **2021**, *60*, 14446–14457.

[16] Yu, L.; Zhou, H. Q.; Sun, J. Y.; Qin, F.; Yu, F.; Bao, J. M.; Yu, Y.; Chen, S.; Ren, Z. F. Cu nanowires shelled with NiFe layered double hydroxide nanosheets as bifunctional electrocatalysts for overall water splitting. *Energy Environ. Sci.* **2017**, *10*, 1820–1827.

[17] Han, A. L.; Zhou, X. F.; Wang, X. J.; Liu, S.; Xiong, Q. H.; Zhang, Q. H.; Gu, L.; Zhuang, Z. C.; Zhang, W. J.; Li, F. X. et al. One-step synthesis of single-site vanadium substitution in 1T-$WS_2$ monolayers for enhanced hydrogen evolution catalysis. *Nat. Commun.* **2021**, *12*, 709.

[18] Guo, Y. N.; Park, T.; Yi, J. W.; Henzie, J.; Kim, J.; Wang, Z. L.; Jiang, B.; Bando, Y.; Sugahara, Y.; Tang, J. et al. Nanoarchitectonics for transition-metal-sulfide-based electrocatalysts for water splitting. *Adv. Mater.* **2019**, *31*, 1807134.

[19] Miao, R.; Dutta, B.; Sahoo, S.; He, J. K.; Zhong, W.; Cetegen, S. A.; Jiang, T.; Alpay, S. P.; Suib, S. L. Mesoporous iron sulfide for highly efficient electrocatalytic hydrogen evolution. *J. Am. Chem. Soc.* **2017**, *139*, 13604–13607.

[20] Tan, Y. W.; Wang, H.; Liu, P.; Shen, Y. H.; Cheng, C.; Hirata, A.; Fujita, T.; Tang, Z.; Chen, M. W. Versatile nanoporous bimetallic phosphides towards electrochemical water splitting. *Energy Environ. Sci.* **2016**, *9*, 2257–2261.

[21] Li, Y.; Dong, Z. H.; Jiao, L. F. Multifunctional transition metal-based phosphides in energy-related electrocatalysis. *Adv. Energy Mater.* **2020**, *10*, 1902104.

[22] Gao, R.; Dai, Q. B.; Du, F.; Yan, D. P.; Dai, L. M. $C_{60}$-adsorbed single-walled carbon nanotubes as metal-free, pH-universal, and multifunctional catalysts for oxygen reduction, oxygen evolution, and hydrogen evolution. *J. Am. Chem. Soc.* **2019**, *141*, 11658–11666.

[23] Fu, N. H.; Liang, X.; Li, Z.; Chen, W. X.; Wang, Y.; Zheng, L. R.; Zhang, Q. H.; Chen, C.; Wang, D. S.; Peng, Q. et al. Fabricating Pd isolated single atom sites on $C_3N_4$/rGO for heterogenization of homogeneous catalysis. *Nano Res.* **2020**, *13*, 947–951.

[24] Sun, X. H.; Tuo, Y. X.; Ye, C. L.; Chen, C.; Lu, Q.; Li, G. N.; Jiang, P.; Chen, S. H.; Zhu, P.; Ma, M. et al. Phosphorus induced electron localization of single iron sites for boosted $CO_2$ electroreduction reaction. *Angew. Chem., Int. Ed.* **2021**, *60*, 23614–23618.

[25] Cui, T. T.; Wang, Y. P.; Ye, T.; Wu, J.; Chen, Z. Q.; Li, J.; Lei, Y. P.; Wang, D. S.; Li, Y. D. Engineering dual single-atom sites on 2D ultrathin N-doped carbon nanosheets attaining ultra-low-temperature zinc-air battery. *Angew. Chem., Int. Ed.* **2022**, *61*, e202115219.

[26] Yang, J. R.; Li, W. H.; Xu, K. N.; Tan, S. D.; Wang, D. S.; Li, Y. D. Regulating the tip effect on single-atom and cluster catalysts: Forming reversible oxygen species with high efficiency in chlorine evolution reaction. *Angew. Chem., Int. Ed.* in press, https://doi.org/10.1002/anie.202200366.

[27] Zhang, P.; Xiang, H. Y.; Tao, L.; Dong, H. J.; Zhou, Y. G.; Hu, T. S.; Chen, X. L.; Liu, S.; Wang, S. Y.; Garaj, S. Chemically activated $MoS_2$ for efficient hydrogen production. *Nano Energy* **2019**, *57*, 535–541.

[28] Anjum, M. A. R.; Jeong, H. Y.; Lee, M. H.; Shin, H. S.; Lee, J. S. Efficient hydrogen evolution reaction catalysis in alkaline media by all-in-one $MoS_2$ with multifunctional active sites. *Adv. Mater.* **2018**, *30*, 1707105.

[29] Kumar, R.; Sahoo, S.; Joanni, E.; Singh, R. K.; Yadav, R. M.; Verma, R. K.; Singh, D. P.; Tan, W. K.; del Pino, A. P.; Moshkalev, S. A. et al. A review on synthesis of graphene, h-BN and $MoS_2$ for energy storage applications: Recent progress and perspectives. *Nano Res.* **2019**, *12*, 2655–2694.

[30] Shah, S. A.; Shen, X. P.; Xie, M. H.; Zhu, G. X.; Ji, Z. Y.; Zhou, H. B.; Xu, K. Q.; Yue, X. Y.; Yuan, A. H.; Zhu, J. et al. Nickel@nitrogen-doped carbon@$MoS_2$ nanosheets: An efficient electrocatalyst for hydrogen evolution reaction. *Small* **2019**, *15*, 1804545.

[31] Nguyen, D. C.; Tran, D. T.; Doan, T. L. L.; Kim, D. H.; Kim, N. H.; Lee, J. H. Rational design of core@shell structured $CoS_x$@$Cu_2MoS_4$ hybridized $MoS_2$/N, S-codoped graphene as advanced electrocatalyst for water splitting and Zn-air battery. *Adv. Energy Mater.* **2020**, *10*, 1903289.

[32] Zhang, J. F.; Wang, Y.; Cui, J. W.; Wu, J. J.; Li, Y.; Zhu, T. Y.; Kang, H. R.; Yang, J. P.; Sun, J.; Qin, Y. Q. et al. Water-soluble defect-rich $MoS_2$ ultrathin nanosheets for enhanced hydrogen evolution. *J. Phys. Chem. Lett.* **2019**, *10*, 3282–3289.

[33] Lukowski, M. A.; Daniel, A. S.; Meng, F.; Forticaux, A.; Li, L. S.; Jin, S. Enhanced hydrogen evolution catalysis from chemically exfoliated metallic $MoS_2$ nanosheets. *J. Am. Chem. Soc.* **2013**, *135*, 10274–10277.

[34] Zhu, D. D.; Liu, J. L.; Zhao, Y. Q.; Zheng, Y.; Qiao, S. Z. Engineering 2D metal-organic framework/$MoS_2$ interface for enhanced alkaline hydrogen evolution. *Small* **2019**, *15*, 1805511.

[35] Dimple; Jena, N.; Rawat, A.; Ahammed, R.; Mohanta, M. K.; De Sarkar, A. Emergence of high piezoelectricity along with robust electron mobility in Janus structures in semiconducting group IVB dichalcogenide monolayers. *J. Mater. Chem. A* **2018**, *6*, 24885–24898.

[36] Zhang, S.; Deng, Q. C.; Shangguan, H. J.; Zheng, C.; Shi, J.; Huang, F. H.; Tang, B. Design and preparation of carbon nitride-based amphiphilic Janus N-doped carbon/$MoS_2$ nanosheets for interfacial enzyme nanoreactor. *ACS Appl. Mater. Interfaces* **2020**, *12*, 12227–12237.

[37] Nguyen, D. C.; Doan, T. L. L.; Prabhakaran, S.; Tran, D. T.; Kim, D. H.; Lee, J. H.; Kim, N. H. Hierarchical Co and Nb dual-doped $MoS_2$ nanosheets shelled micro-$TiO_2$ hollow spheres as effective multifunctional electrocatalysts for HER, OER, and ORR. *Nano Energy* **2021**, *82*, 105750.

[38] Yu, X. Y.; Hu, H.; Wang, Y. W.; Chen, H. Y.; Lou, X. W. Ultrathin $MoS_2$ nanosheets supported on N-doped carbon nanoboxes with enhanced lithium storage and electrocatalytic properties. *Angew. Chem., Int. Ed.* **2015**, *54*, 7395–7398.

[39] Gong, F. L.; Liu, M. M.; Ye, S.; Gong, L. H.; Zeng, G.; Xu, L.; Zhang, X. L.; Zhang, Y. H.; Zhou, L. M.; Fang, S. M. et al. All-pH stable sandwich-structured $MoO_2$/$MoS_2$/C hollow nanoreactors for enhanced electrochemical hydrogen evolution. *Adv. Funct. Mater.* **2021**, *31*, 2101715.

[40] Chen, J. Z.; Liu, G. G.; Zhu, Y. Z.; Su, M.; Yin, P. F.; Wu, X. J.; Lu, Q. P.; Tan, C. L.; Zhao, M. T.; Liu, Z. Q. et al. Ag@$MoS_2$ core−shell heterostructure as SERS platform to reveal the hydrogen evolution active sites of single-layer $MoS_2$. *J. Am. Chem. Soc.* **2020**, *142*, 7161–7167.

[41] Qin, Q.; Chen, L. L.; Wei, T.; Liu, X. E. $MoS_2$/NiS yolk−shell microsphere-based electrodes for overall water splitting and

asymmetric supercapacitor. *Small* **2019**, *15*, 1803639.
[42] Zhang, Q. Q.; Bai, H.; Zhang, Q.; Ma, Q.; Li, Y. H.; Wan, C. Q.; Xi, G. C. $MoS_2$ yolk−shell microspheres with a hierarchical porous structure for efficient hydrogen evolution. *Nano Res.* **2016**, *9*, 3038–3047.
[43] Gong, F. L.; Ye, S.; Liu, M. M.; Zhang, J. W.; Gong, L. H.; Zeng, G.; Meng, E. C.; Su, P. P.; Xie, K. F.; Zhang, Y. H. et al. Boosting electrochemical oxygen evolution over yolk-shell structured O-$MoS_2$ nanoreactors with sulfur vacancy and decorated Pt nanoparticles. *Nano Energy* **2020**, *78*, 105284.
[44] Hu, H.; Han, L.; Yu, M. Z.; Wang, Z. Y.; Lou, X. W. Metal-organic-framework-engaged formation of Co nanoparticle-embedded carbon@$Co_9S_8$ double-shelled nanocages for efficient oxygen reduction. *Energy Environ. Sci.* **2016**, *9*, 107–111.
[45] Wan, Y.; Zhang, Z. Y.; Xu, X. L.; Zhang, Z. H.; Li, P.; Fang, X.; Zhang, K.; Yuan, K.; Liu, K. H.; Ran, G. Z. et al. Engineering active edge sites of fractal-shaped single-layer $MoS_2$ catalysts for high-efficiency hydrogen evolution. *Nano Energy* **2018**, *51*, 786–792.
[46] Li, Y.; Zuo, S. W.; Li, Q. H.; Wu, X.; Zhang, J.; Zhang, H. B.; Zhang, J. Vertically aligned $MoS_2$ with in-plane selectively cleaved Mo−S bond for hydrogen production. *Nano Lett.* **2021**, *21*, 1848–1855.
[47] Zhang, J.; Wang, T.; Pohl, D.; Rellinghaus, B.; Dong, R. H.; Liu, S. H.; Zhuang, X. D.; Feng, X. L. Interface engineering of $MoS_2$/$Ni_3S_2$ heterostructures for highly enhanced electrochemical overall-water-splitting activity. *Angew. Chem., Int. Ed.* **2016**, *55*, 6702–6707.
[48] Yu, X. Y.; Feng, Y.; Jeon, Y.; Guan, B. Y.; Lou, X. W.; Paik, U. Formation of Ni-Co-$MoS_2$ nanoboxes with enhanced electrocatalytic activity for hydrogen evolution. *Adv. Mater.* **2016**, *28*, 9006–9011.
[49] Lin, J. H.; Wang, P. C.; Wang, H. H.; Li, C.; Si, X. Q.; Qi, J. L.; Cao, J.; Zhong, Z. X.; Fei, W. D.; Feng, J. C. Defect-rich heterogeneous $MoS_2$/$NiS_2$ nanosheets electrocatalysts for efficient overall water splitting. *Adv. Sci.* **2019**, *6*, 1900246.
[50] Lu, A. Y.; Yang, X. L.; Tseng, C. C.; Min, S. X.; Lin, S. H.; Hsu, C. L.; Li, H. N.; Idriss, H.; Kuo, J. L.; Huang, K. W. et al. High-sulfur-vacancy amorphous molybdenum sulfide as a high current electrocatalyst in hydrogen evolution. *Small* **2016**, *12*, 5530–5537.
[51] Tan, C. L.; Luo, Z. M.; Chaturvedi, A.; Cai, Y. Q.; Du, Y. H.; Gong, Y.; Huang, Y.; Lai, Z. C.; Zhang, X.; Zheng, L. R. et al. Preparation of high-percentage 1T-phase transition metal dichalcogenide nanodots for electrochemical hydrogen evolution. *Adv. Mater.* **2018**, *30*, 1705509.
[52] Zheng, Z. L.; Yu, L.; Gao, M.; Chen, X. Y.; Zhou, W.; Ma, C.; Wu, L. H.; Zhu, J. F.; Meng, X. Y.; Hu, J. T. et al. Boosting hydrogen evolution on $MoS_2$ via co-confining selenium in surface and cobalt in inner layer. *Nat. Commun.* **2020**, *11*, 3315.
[53] Solomon, G.; Kohan, M. G.; Vagin, M.; Rigoni, F.; Mazzaro, R.; Natile, M. M.; You, S. J.; Morandi, V.; Concina, I.; Vomiero, A. Decorating vertically aligned $MoS_2$ nanoflakes with silver nanoparticles for inducing a bifunctional electrocatalyst towards oxygen evolution and oxygen reduction reaction. *Nano Energy* **2021**, *81*, 105664.
[54] Kuang, P. Y.; Tong, T.; Fan, K.; Yu, J. G. *In situ* fabrication of Ni-Mo bimetal sulfide hybrid as an efficient electrocatalyst for hydrogen evolution over a wide pH range. *ACS Catal.* **2017**, *7*, 6179–6187.
[55] Jian, W. J.; Cheng, X. L.; Huang, Y. Y.; You, Y.; Zhou, R.; Sun, T. T.; Xu, J. Arrays of ZnO/$MoS_2$ nanocables and $MoS_2$ nanotubes with phase engineering for bifunctional photoelectrochemical and electrochemical water splitting. *Chem. Eng. J.* **2017**, *328*, 474–483.
[56] Luo, M.; Liu, S. Q.; Zhu, W. W.; Ye, G. Y.; Wang, J.; He, Z. An electrodeposited $MoS_2$−$MoO_{3-x}$/$Ni_3S_2$ heterostructure electrocatalyst for efficient alkaline hydrogen evolution. *Chem. Eng. J.* **2022**, *428*, 131055.
[57] Zhou, Y.; Hao, W.; Zhao, X. X.; Zhou, J. D.; Yu, H. M.; Lin, B.; Liu, Z.; Pennycook, S. J.; Li, S. Z.; Fan, H. J. Electronegativity-induced charge balancing to boost stability and activity of amorphous electrocatalysts. *Adv. Mater.*, in press, https://doi.org/10.1002/adma.202100537.
[58] Wu, T.; Song, E. H.; Zhang, S. N.; Luo, M. J.; Zhao, C. D.; Zhao, W.; Liu, J. J.; Huang, F. Q. Engineering metallic heterostructure based on $Ni_3N$ and 2M-$MoS_2$ for alkaline water electrolysis with industry-compatible current density and stability. *Adv. Mater.* **2022**, *34*, 2108505.
[59] Li, R. Z.; Wang, D. S. Superiority of dual-atom catalysts in electrocatalysis: One step further than single-atom catalysts. *Adv. Energy Mater.* **2022**, *12*, 2103564.
[60] Qi, K.; Cui, X. Q.; Gu, L.; Yu, S. S.; Fan, X. F.; Luo, M. C.; Xu, S.; Li, N. B.; Zheng, L. R.; Zhang, Q. H. et al. Single-atom cobalt array bound to distorted 1T $MoS_2$ with ensemble effect for hydrogen evolution catalysis. *Nat. Commun.* **2019**, *10*, 5231.
[61] Zhang, J. M.; Xu, X. P.; Yang, L.; Cheng, D. J.; Cao, D. P. Single-atom Ru doping induced phase transition of $MoS_2$ and S vacancy for hydrogen evolution reaction. *Small Methods* **2019**, *3*, 1900653.
[62] Wang, Y.; Zheng, X. B.; Wang, D. S. Design concept for electrocatalysts. *Nano Res.* **2022**, *15*, 1730–1752.
[63] Wei, H.; Si, J. C.; Zeng, L. B.; Lyu, S. L.; Zhang, Z. G.; Suo, Y. G.; Hou, Y. Electrochemically exfoliated Ni-doped $MoS_2$ nanosheets for highly efficient hydrogen evolution and Zn-$H_2O$ battery. *Chin. Chem. Lett.*, in press, https://doi.org/10.1016/j.cclet.2022.01.037.
[64] Zheng, M. Y.; Guo, K. L.; Jiang, W. J.; Tang, T.; Wang, X. Y.; Zhou, P. P.; Du, J.; Zhao, Y. Q.; Xu, C. L.; Hu, J. S. When $MoS_2$ meets FeOOH: A "one-stone-two-birds" heterostructure as a bifunctional electrocatalyst for efficient alkaline water splitting. *Appl. Catal. B:Environ.* **2019**, *244*, 1004–1012.
[65] Yin, J.; Jin, J.; Lin, H. H.; Yin, Z. Y.; Li, J. Y.; Lu, M.; Guo, L. C.; Xi, P. X.; Tang, Y.; Yan, C. H. Optimized metal chalcogenides for boosting water splitting. *Adv. Sci.* **2020**, *7*, 1903070.
[66] Sun, K. A.; Zeng, L. Y.; Liu, S. H.; Zhao, L.; Zhu, H. Y.; Zhao, J. C.; Liu, Z.; Cao, D. W.; Hou, Y. C.; Liu, Y. Q. et al. Design of basal plane active $MoS_2$ through one-step nitrogen and phosphorus co-doping as an efficient pH-universal electrocatalyst for hydrogen evolution. *Nano Energy* **2019**, *58*, 862–869.
[67] Xie, J. F.; Zhang, H.; Li, S.; Wang, R. X.; Sun, X.; Zhou, M.; Zhou, J. F.; Lou, X. W.; Xie, Y. Defect-rich $MoS_2$ ultrathin nanosheets with additional active edge sites for enhanced electrocatalytic hydrogen evolution. *Adv. Mater.* **2013**, *25*, 5807–5813.
[68] Li, G. Q.; Zhang, D.; Qiao, Q.; Yu, Y. F.; Peterson, D.; Zafar, A.; Kumar, R.; Curtarolo, S.; Hunte, F.; Shannon, S. et al. All the catalytic active sites of $MoS_2$ for hydrogen evolution. *J. Am. Chem. Soc.* **2016**, *138*, 16632–16638.
[69] Ma, Q.; Qiao, H.; Huang, Z. Y.; Liu, F.; Duan, C. G.; Zhou, Y.; Liao, G. C.; Qi, X. Photo-assisted electrocatalysis of black phosphorus quantum dots/molybdenum disulfide heterostructure for oxygen evolution reaction. *Appl. Surf. Sci.* **2021**, *562*, 150213.
[70] Zhang, G.; Liu, H. J.; Qu, J. H.; Li, J. H. Two-dimensional layered $MoS_2$: Rational design, properties and electrochemical applications. *Energy Environ. Sci.* **2016**, *9*, 1190–1209.
[71] Wang, Y. F.; Yu, Y.; Wang, J. L.; Peng, L. H.; Zuo, Y. X.; Zuo, C. C. Novel multifunctional Janus-type membrane on Al anode for corrosion protection. *Adv. Mater. Interfaces* **2021**, *8*, 2100786.
[72] Lu, A. Y.; Zhu, H. Y.; Xiao, J.; Chuu, C. P.; Han, Y. M.; Chiu, M. H.; Cheng, C. C.; Yang, C. W.; Wei, K. H.; Yang, Y. M. et al. Janus monolayers of transition metal dichalcogenides. *Nat. Nanotechnol.* **2017**, *12*, 744–749.
[73] Zhou, L.; Zhang, H. W.; Bao, H. M.; Wei, Y.; Fu, H.; Cai, W. P. Monodispersed snowman-like Ag-$MoS_2$ Janus nanoparticles as chemically self-propelled nanomotors. *ACS Appl. Nano Mater.* **2020**, *3*, 624–632.
[74] Zhou, L.; Zhang, H. W.; Bao, H. M.; Liu, G. Q.; Li, Y.; Cai, W. P. Decoration of Au nanoparticles on $MoS_2$ nanospheres: From Janus to core/shell structure. *J. Phys. Chem. C* **2018**, *122*, 8628–8636.
[75] Zhang, K. Y.; Guo, Y. F.; Larson, D. T.; Zhu, Z. Y.; Fang, S. A.; Kaxiras, E.; Kong, J.; Huang, S. X. Spectroscopic signatures of interlayer coupling in Janus MoSSe/$MoS_2$ heterostructures. *ACS Nano* **2021**, *15*, 14394–14403.
[76] Wang, J. Y.; Cui, Y.; Wang, D. Design of hollow nanostructures for energy storage, conversion and production. *Adv. Mater.* **2019**, *31*,

1801993.
[77] Zhang, L.; Wu, H. B.; Yan, Y.; Wang, X.; Lou, X. W. Hierarchical $MoS_2$ microboxes constructed by nanosheets with enhanced electrochemical properties for lithium storage and water splitting. *Energy Environ. Sci.* **2014**, *7*, 3302–3306.
[78] Tang, B. S.; Yu, Z. G.; Zhang, Y. X.; Tang, C. H.; Seng, H. L.; Seh, Z. W.; Zhang, Y. W.; Pennycook, S. J.; Gong, H.; Yang, W. F. Metal-organic framework-derived hierarchical $MoS_2/CoS_2$ nanotube arrays as pH-universal electrocatalysts for efficient hydrogen evolution. *J. Mater. Chem. A* **2019**, *7*, 13339–13346.
[79] Li, H. H.; Yu, S. H. Recent advances on controlled synthesis and engineering of hollow alloyed nanotubes for electrocatalysis. *Adv. Mater.* **2019**, *31*, 1803503.
[80] Wang, C.; Zhang, L.; Xu, G. C.; Yang, L. F.; Yang, J. H. Construction of unique ternary composite MCNTs@$CoS_x$@$MoS_2$ with three-dimensional lamellar heterostructure as high-performance bifunctional electrocatalysts for hydrogen evolution and oxygen evolution reactions. *Chem. Eng. J.* **2021**, *417*, 129270.
[81] Li, Y. J.; Wang, W. Y.; Huang, B. J.; Mao, Z. F.; Wang, R.; He, B. B.; Gong, Y. S.; Wang, H. W. Abundant heterointerfaces in MOF-derived hollow $CoS_2$-$MoS_2$ nanosheet array electrocatalysts for overall water splitting. *J. Energy Chem.* **2021**, *57*, 99–108.
[82] Kim, M.; Seok, H.; Selvam, N. C. S.; Cho, J.; Choi, G. H.; Nam, M. G.; Kang, S.; Kim, T.; Yoo, P. J. Kirkendall effect induced bifunctional hybrid electrocatalyst ($Co_9S_8$@$MoS_2$/N-doped hollow carbon) for high performance overall water splitting. *J. Power Sources* **2021**, *493*, 229688.
[83] Guo, Y. N.; Tang, J.; Wang, Z. L.; Kang, Y. M.; Bando, Y.; Yamauchi, Y. Elaborately assembled core-shell structured metal sulfides as a bifunctional catalyst for highly efficient electrochemical overall water splitting. *Nano Energy* **2018**, *47*, 494–502.
[84] Li, Y.; Majewski, M. B.; Islam, S. M.; Hao, S. Q.; Murthy, A. A.; DiStefano, J. G.; Hanson, E. D.; Xu, Y. B.; Wolverton, C.; Kanatzidis, M. G. et al. Morphological engineering of winged Au@$MoS_2$ heterostructures for electrocatalytic hydrogen evolution. *Nano Lett.* **2018**, *18*, 7104–7110.
[85] Zhu, H.; Gao, G. H.; Du, M. L.; Zhou, J. H.; Wang, K.; Wu, W. B.; Chen, X.; Li, Y.; Ma, P. M.; Dong, W. F. et al. Atomic-scale core/shell structure engineering induces precise tensile strain to boost hydrogen evolution catalysis. *Adv. Mater.* **2018**, *30*, 1707301.
[86] Zhu, H.; Zhang, J. F.; Yanzhang, R. P.; Du, M. L.; Wang, Q. F.; Gao, G. H.; Wu, J. D.; Wu, G. M.; Zhang, M.; Liu, B. et al. When cubic cobalt sulfide meets layered molybdenum disulfide: A core−shell system toward synergetic electrocatalytic water splitting. *Adv. Mater.* **2015**, *27*, 4752–4759.
[87] Doan, T. L. L.; Nguyen, D. C.; Prabhakaran, S.; Kim, D. H.; Tran, D. T.; Kim, N. H.; Lee, J. H. Single-atom Co-decorated $MoS_2$ nanosheets assembled on metal nitride nanorod arrays as an efficient bifunctional electrocatalyst for pH-universal water splitting. *Adv. Funct. Mater.* **2021**, *31*, 2100233.
[88] Zhang, Q.; Liu, B. Q.; Ji, Y.; Chen, L. H.; Zhang, L. Y.; Li, L.; Wang, C. G. Construction of hierarchical yolk−shell nanospheres organized by ultrafine Janus subunits for efficient overall water splitting. *Nanoscale* **2020**, *12*, 2578–2586.
[89] Wu, A. P.; Tian, C. G.; Yan, H. J.; Jiao, Y. Q.; Yan, Q.; Yang, G. Y.; Fu, H. G. Hierarchical $MoS_2$@MoP core−shell heterojunction electrocatalysts for efficient hydrogen evolution reaction over a broad pH range. *Nanoscale* **2016**, *8*, 11052–11059.
[90] Bai, J. M.; Meng, T.; Guo, D. L.; Wang, S. G.; Mao, B. G.; Cao, M. H. $Co_9S_8$@$MoS_2$ core−shell heterostructures as trifunctional electrocatalysts for overall water splitting and Zn-air batteries. *ACS Appl. Mater. Interfaces* **2018**, *10*, 1678–1689.
[91] Xing, Z. C.; Yang, X. R.; Asiri, A. M.; Sun, X. P. Three-dimensional structures of $MoS_2$@Ni core/shell nanosheets array toward synergetic electrocatalytic water splitting. *ACS Appl. Mater. Interfaces* **2016**, *8*, 14521–14526.
[92] Yang, T.; Yin, L. S.; He, M. S.; Wei, W. X.; Cao, G. J.; Ding, X. R.; Wang, Y. H.; Zhao, Z. M.; Yu, T. T.; Zhao, H. et al. Yolk−shell hierarchical catalyst with tremella-like molybdenum sulfide on transition metal (Co, Ni and Fe) sulfide for electrochemical water splitting. *Chem. Commun.* **2019**, *55*, 14343–14346.
[93] Liu, P. T.; Zhu, J. Y.; Zhang, J. Y.; Xi, P. X.; Tao, K.; Gao, D. Q.; Xue, D. S. P dopants triggered new basal plane active sites and enlarged interlayer spacing in $MoS_2$ nanosheets toward electrocatalytic hydrogen evolution. *ACS Energy Lett.* **2017**, *2*, 745–752.
[94] Zang, Y. P.; Niu, S. W.; Wu, Y. S.; Zheng, X. S.; Cai, J. Y.; Ye, J.; Xie, Y. F.; Liu, Y.; Zhou, J. B.; Zhu, J. F. et al. Tuning orbital orientation endows molybdenum disulfide with exceptional alkaline hydrogen evolution capability. *Nat. Commun.* **2019**, *10*, 1217.
[95] Deng, S. J.; Luo, M.; Ai, C. Z.; Zhang, Y.; Liu, B.; Huang, L.; Jiang, Z.; Zhang, Q. H.; Gu, L.; Lin, S. W. et al. Synergistic doping and intercalation: Realizing deep phase modulation on $MoS_2$ arrays for high-efficiency hydrogen evolution reaction. *Angew. Chem., Int. Ed.* **2019**, *58*, 16289–16296.
[96] Xiong, J.; Li, J.; Shi, J. W.; Zhang, X. L.; Cai, W. W.; Yang, Z. H.; Cheng, H. S. Metallic 1T-$MoS_2$ nanosheets *in-situ* entrenched on N, P, S-co doped hierarchical carbon microflower as an efficient and robust electro-catalyst for hydrogen evolution. *Appl. Catal. B:Environ.* **2019**, *243*, 614–620.
[97] Luo, Z. Y.; Ouyang, Y. X.; Zhang, H.; Xiao, M. L.; Ge, J. J.; Jiang, Z.; Wang, J. L.; Tang, D. M.; Cao, X. Z.; Liu, C. P. et al. Chemically activating $MoS_2$ via spontaneous atomic palladium interfacial doping towards efficient hydrogen evolution. *Nat. Commun.* **2018**, *9*, 2120.
[98] Shi, Y.; Zhou, Y.; Yang, D. R.; Xu, W. X.; Wang, C.; Wang, F. B.; Xu, J. J.; Xia, X. H.; Chen, H. Y. Energy level engineering of $MoS_2$ by transition-metal doping for accelerating hydrogen evolution reaction. *J. Am. Chem. Soc.* **2017**, *139*, 15479–15485.
[99] Yang, S. Z.; Gong, Y. J.; Manchanda, P.; Zhang, Y. Y.; Ye, G. L.; Chen, S. M.; Song, L.; Pantelides, S. T.; Ajayan, P. M.; Chisholm, M. F. et al. Rhenium-doped and stabilized $MoS_2$ atomic layers with basal-plane catalytic activity. *Adv. Mater.* **2018**, *30*, 1803477.
[100] Li, Y.; Gu, Q. F.; Johannessen, B.; Zheng, Z.; Li, C.; Luo, Y. T.; Zhang, Z. Y.; Zhang, Q.; Fan, H. N.; Luo, W. B. et al. Synergistic Pt doping and phase conversion engineering in two-dimensional $MoS_2$ for efficient hydrogen evolution. *Nano Energy* **2021**, *84*, 105898.
[101] Sun, T.; Wang, J.; Chi, X.; Lin, Y. X.; Chen, Z. X.; Ling, X.; Qiu, C. T.; Xu, Y. S.; Song, L.; Chen, W. et al. Engineering the electronic structure of $MoS_2$ nanorods by N and Mn dopants for ultra-efficient hydrogen production. *ACS Catal.* **2018**, *8*, 7585–7592.
[102] Wei, C.; Wu, W. Z.; Li, H.; Lin, X. C.; Wu, T.; Zhang, Y. D.; Xu, Q.; Zhang, L. P.; Zhu, Y. H.; Yang, X. N. et al. Atomic plane-vacancy engineering of transition-metal dichalcogenides with enhanced hydrogen evolution capability. *ACS Appl. Mater. Interfaces* **2019**, *11*, 25264–25270.
[103] Yin, Y.; Han, J. C.; Zhang, Y. M.; Zhang, X. H.; Xu, P.; Yuan, Q.; Samad, L.; Wang, X. J.; Wang, Y.; Zhang, Z. H. et al. Contributions of phase, sulfur vacancies, and edges to the hydrogen evolution reaction catalytic activity of porous molybdenum disulfide nanosheets. *J. Am. Chem. Soc.* **2016**, *138*, 7965–7972.
[104] Wu, W. Z.; Niu, C. Y.; Wei, C.; Jia, Y.; Li, C.; Xu, Q. Activation of $MoS_2$ basal planes for hydrogen evolution by zinc. *Angew. Chem., Int. Ed.* **2019**, *58*, 2029–2033.
[105] Deng, J.; Li, H. B.; Wang, S. H.; Ding, D.; Chen, M. S.; Liu, C.; Tian, Z. Q.; Novoselov, K. S.; Ma, C.; Deng, D. H. et al. Multiscale structural and electronic control of molybdenum disulfide foam for highly efficient hydrogen production. *Nat. Commun.* **2017**, *8*, 14430.
[106] Luo, Z. Y.; Zhang, H.; Yang, Y. Q.; Wang, X.; Li, Y.; Jin, Z.; Jiang, Z.; Liu, C. P.; Xing, W.; Ge, J. J. Reactant friendly hydrogen evolution interface based on di-anionic $MoS_2$ surface. *Nat. Commun.* **2020**, *11*, 1116.
[107] Cheng, Y. F.; Lu, S. K.; Liao, F.; Liu, L. B.; Li, Y. Q.; Shao, M. W. Rh-$MoS_2$ nanocomposite catalysts with Pt-like activity for hydrogen evolution reaction. *Adv. Funct. Mater.* **2017**, *27*, 1700359.
[108] Li, H.; Tsai, C.; Koh, A. L.; Cai, L. L.; Contryman, A. W.; Fragapane, A. H.; Zhao, J. H.; Han, H. S.; Manoharan, H. C.; Abild-

Pedersen, F. et al. Activating and optimizing $MoS_2$ basal planes for hydrogen evolution through the formation of strained sulphur vacancies. *Nat. Mater.* **2016**, *15*, 48–53.
[109] Yang, J.; Wang, Y.; Lagos, M. J.; Manichev, V.; Fullon, R.; Song, X. J.; Voiry, D.; Chakraborty, S.; Zhang, W. J.; Batson, P. E. et al. Single atomic vacancy catalysis. *ACS Nano* **2019**, *13*, 9958–9964.
[110] Wang, X.; Zhang, Y. W.; Si, H. N.; Zhang, Q. H.; Wu, J.; Gao, L.; Wei, X. F.; Sun, Y.; Liao, Q. L.; Zhang, Z. et al. Single-atom vacancy defect to trigger high-efficiency hydrogen evolution of $MoS_2$. *J. Am. Chem. Soc.* **2020**, *142*, 4298–4308.
[111] Cheng, Z. H.; Xiao, Y. K.; Wu, W. P.; Zhang, X. Q.; Fu, Q.; Zhao, Y.; Qu, L. T. All-pH-tolerant in-plane heterostructures for efficient hydrogen evolution reaction. *ACS Nano* **2021**, *15*, 11417–11427.
[112] Wu, Y.; Li, F.; Chen, W. L.; Xiang, Q.; Ma, Y. L.; Zhu, H.; Tao, P.; Song, C. Y.; Shang, W.; Deng, T. et al. Coupling interface constructions of $MoS_2/Fe_5Ni_4S_8$ heterostructures for efficient electrochemical water splitting. *Adv. Mater.* **2018**, *30*, 1803151.
[113] Muthurasu, A.; Maruthapandian, V.; Kim, H. Y. Metal-organic framework derived $Co_3O_4/MoS_2$ heterostructure for efficient bifunctional electrocatalysts for oxygen evolution reaction and hydrogen evolution reaction. *Appl. Catal. B:Environ.* **2019**, *248*, 202–210.
[114] Ji, X. X.; Lin, Y. H.; Zeng, J.; Ren, Z. H.; Lin, Z. J.; Mu, Y. B.; Qiu, Y. J.; Yu, J. Graphene/$MoS_2$/$FeCoNi(OH)_x$ and graphene/$MoS_2$/$FeCoNiP_x$ multilayer-stacked vertical nanosheets on carbon fibers for highly efficient overall water splitting. *Nat. Commun.* **2021**, *12*, 1380.
[115] Lim, K. R. G.; Handoko, A. D.; Johnson, L. R.; Meng, X.; Lin, M.; Subramanian, G. S.; Anasori, B.; Gogotsi, Y.; Vojvodic, A.; Seh, Z. W. 2H-$MoS_2$ on $Mo_2CT_x$MXene nanohybrid for efficient and durable electrocatalytic hydrogen evolution. *ACS Nano* **2020**, *14*, 16140–16155.
[116] Kim, M.; Anjum, M. A. R.; Lee, M.; Lee, B. J.; Lee, J. S. Activating $MoS_2$ basal plane with $Ni_2P$ nanoparticles for Pt-like hydrogen evolution reaction in acidic media. *Adv. Funct. Mater.* **2019**, *29*, 1809151.
[117] Li, H. Y.; Chen, S. M.; Jia, X. F.; Xu, B.; Lin, H. F.; Yang, H. Z.; Song, L.; Wang, X. Amorphous nickel-cobalt complexes hybridized with 1T-phase molybdenum disulfide via hydrazine-induced phase transformation for water splitting. *Nat. Commun.* **2017**, *8*, 15377.
[118] Zhai, Z. J.; Li, C.; Zhang, L.; Wu, H. C.; Zhang, L.; Tang, N.; Wang, W.; Gong, J. L. Dimensional construction and morphological tuning of heterogeneous $MoS_2$/NiS electrocatalysts for efficient overall water splitting. *J. Mater. Chem. A* **2018**, *6*, 9833–9838.
[119] Chang, P.; Zhang, S.; Xu, X. M.; Lin, Y. F.; Chen, X. Y.; Guan, L. X.; Tao, J. G. Facile synthesis of $MoS_2/Ni_2V_3O_8$ nanosheets for pH-universal efficient hydrogen evolution catalysis. *Chem. Eng. J.* **2021**, *423*, 130196.
[120] Mao, H.; Guo, X.; Fan, Q. Z.; Fu, Y. L.; Yang, H. R.; Liu, D. L.; Wu, S. Y.; Wu, Q.; Song, X. M. Improved hydrogen evolution activity by unique $NiS_2$−$MoS_2$ heterostructures with misfit lattices supported on poly(ionic liquid)s functionalized polypyrrole/graphene oxide nanosheets. *Chem. Eng. J.* **2021**, *404*, 126253.
[121] Qin, C. L.; Fan, A. X.; Zhang, X.; Wang, S. Q.; Yuan, X. L.; Dai, X. P. Interface engineering: Few-layer $MoS_2$ coupled to a NiCo-sulfide nanosheet heterostructure as a bifunctional electrocatalyst for overall water splitting. *J. Mater. Chem. A* **2019**, *7*, 27594–27602.
[122] Lei, L.; Huang, D. L.; Lai, C.; Zhang, C.; Deng, R.; Chen, Y. S.; Chen, S.; Wang, W. J. Interface modulation of $Mo_2C$@foam nickel via $MoS_2$ quantum dots for the electrochemical oxygen evolution reaction. *J. Mater. Chem. A* **2020**, *8*, 15074–15085.
[123] Tang, Y. J.; Wang, Y.; Wang, X. L.; Li, S. L.; Huang, W.; Dong, L. Z.; Liu, C. H.; Li, Y. F.; Lan, Y. Q. Molybdenum disulfide/nitrogen-doped reduced graphene oxide nanocomposite with enlarged interlayer spacing for electrocatalytic hydrogen evolution. *Adv. Energy Mater.* **2016**, *6*, 1600116.
[124] Ibupoto, Z. H.; Tahira, A.; Tang, P. Y.; Liu, X. J.; Morante, J. R.; Fahlman, M.; Arbiol, J.; Vagin, M.; Vomiero, A. $MoS_x$@NiO composite nanostructures: An advanced nonprecious catalyst for hydrogen evolution reaction in alkaline media. *Adv. Funct. Mater.* **2019**, *29*, 1807562.
[125] Zhang, X.; Liang, Y. Y. Nickel hydr(oxy)oxide nanoparticles on metallic $MoS_2$ nanosheets: A synergistic electrocatalyst for hydrogen evolution reaction. *Adv. Sci.* **2018**, *5*, 1700644.
[126] Ji, D. X.; Peng, S. J.; Fan, L.; Li, L. L.; Qin, X. H.; Ramakrishna, S. Thin $MoS_2$ nanosheets grafted MOFs-derived porous Co-N-C flakes grown on electrospun carbon nanofibers as self-supported bifunctional catalysts for overall water splitting. *J. Mater. Chem. A* **2017**, *5*, 23898–23908.
[127] Lei, Y. P.; Wang, Y. C.; Liu, Y.; Song, C. Y.; Li, Q.; Wang, D. S.; Li, Y. D, Design aktiver atomarer zentren für HER-elektrokatalysatoren. *Angew. Chem., Int. Ed.* **2020**, *132*, 20978–20998.
[128] Chen, S. H.; Li, W. H.; Jiang, W. J.; Yang, J. R.; Zhu, J. X.; Wang, L. Q.; Ou, H. H.; Zhuang, Z. C.; Chen, M. Z.; Sun, X. H. et al. MOF encapsulating N-heterocyclic carbene-ligated copper single-atom site catalyst towards efficient methane electrosynthesis. *Angew. Chem., Int. Ed.* **2022**, *61*, e202114450.
[129] Liu, Y. W.; Wang, B. X.; Fu, Q.; Liu, W.; Wang, Y.; Gu, L.; Wang, D. S.; Li, Y. D. Polyoxometalate-based metal-organic framework as molecular sieve for highly selective semi-hydrogenation of acetylene on isolated single Pd atom sites. *Angew. Chem., Int. Ed.* **2021**, *60*, 22522–22528.
[130] Jiang, K.; Luo, M.; Liu, Z. X.; Peng, M.; Chen, D. C.; Lu, Y. R.; Chan, T. S.; de Groot, F. M. F.; Tan, Y. W. Rational strain engineering of single-atom ruthenium on nanoporous $MoS_2$ for highly efficient hydrogen evolution. *Nat. Commun.* **2021**, *12*, 1687.
[131] Wang, J.; Fang, W. H.; Hu, Y.; Zhang, Y. H.; Dang, J. Q.; Wu, Y.; Chen, B. Z.; Zhao, H.; Li, Z. X. Single atom Ru doping 2H-$MoS_2$ as highly efficient hydrogen evolution reaction electrocatalyst in a wide pH range. *Appl. Catal. B:Environ.* **2021**, *298*, 120490.
[132] Ji, L.; Yan, P. F.; Zhu, C. H.; Ma, C. Y.; Wu, W. Z.; Wei, C.; Shen, Y. L.; Chu, S. Q.; Wang, J. O.; Du, Y. et al. One-pot synthesis of porous 1T-phase $MoS_2$ integrated with single-atom Cu doping for enhancing electrocatalytic hydrogen evolution reaction. *Appl. Catal. B: Environ.* **2019**, *251*, 87–93.
[133] Meng, X. Y.; Ma, C.; Jiang, L. Z.; Si, R.; Meng, X. G.; Tu, Y. C.; Yu, L.; Bao, X. H.; Deng, D. H. Distance synergy of $MoS_2$-confined rhodium atoms for highly efficient hydrogen evolution. *Angew. Chem., Int. Ed.* **2020**, *132*, 10588–10593.
[134] Li, X. Y.; Rong, H. P.; Zhang, J. T.; Wang, D. S.; Li, Y. D. Modulating the local coordination environment of single-atom catalysts for enhanced catalytic performance. *Nano Res.* **2020**, *13*, 1842–1855.
[135] Zhai, P. L.; Zhang, Y. X.; Wu, Y. Z.; Gao, J. F.; Zhang, B.; Cao, S. Y.; Zhang, Y. T.; Li, Z. W.; Sun, L. C.; Hou, J. G. Engineering active sites on hierarchical transition bimetal oxides/sulfides heterostructure array enabling robust overall water splitting. *Nat. Commun.* **2020**, *11*, 5462.
[136] Xiong, Q. Z.; Wang, Y.; Liu, P. F.; Zheng, L. R.; Wang, G. Z.; Yang, H. G.; Wong, P. K.; Zhang, H. M.; Zhao, H. J. Cobalt covalent doping in $MoS_2$ to induce bifunctionality of overall water splitting. *Adv. Mater.* **2018**, *30*, 1801450.
[137] Yang, Y. Q.; Zhang, K.; Ling, H. L.; Li, X.; Chan, H. C.; Yang, L. C.; Gao, Q. S. $MoS_2$−$Ni_3S_2$ heteronanorods as efficient and stable bifunctional electrocatalysts for overall water splitting. *ACS Catal.* **2017**, *7*, 2357–2366.
[138] Kwon, I. S.; Debela, T. T.; Kwak, I. H.; Park, Y. C.; Seo, J.; Shim, J. Y.; Yoo, S. J.; Kim, J. G.; Park, J.; Kang, H. S. Ruthenium nanoparticles on cobalt-doped 1T' phase $MoS_2$ nanosheets for overall water splitting. *Small* **2020**, *16*, 2000081.
[139] Kuang, P. Y.; He, M.; Zou, H. Y.; Yu, J. G.; Fan, K. 0D/3D $MoS_2$-$NiS_2$/N-doped graphene foam composite for efficient overall water splitting. *Appl. Catal. B:Environ.* **2019**, *254*, 15–25.
[140] Yoon, T.; Kim, K. S. One-step synthesis of CoS-doped β-

$Co(OH)_2$@amorphous $MoS_{2+x}$ hybrid catalyst grown on nickel foam for high-performance electrochemical overall water splitting. *Adv. Funct. Mater.* **2016**, *26*, 7386–7393.

[141] Lu, Y. K.; Guo, X. X.; Yang, L. Y.; Yang, W. F.; Sun, W. T.; Tuo, Y. X.; Zhou, Y.; Wang, S. T.; Pan, Y.; Yan, W. F. et al. Highly efficient CoMoS heterostructure derived from vertically anchored $Co_5Mo_{10}$ polyoxometalate for electrocatalytic overall water splitting. *Chem. Eng. J.* **2020**, *394*, 124849.

[142] Liu, Y. K.; Jiang, S.; Li, S. J.; Zhou, L.; Li, Z. H.; Li, J. M.; Shao, M. F. Interface engineering of (Ni, Fe)$S_2$@$MoS_2$ heterostructures for synergetic electrochemical water splitting. *Appl. Catal. B:Environ.* **2019**, *247*, 107–114.

[143] Wei, S. T.; Cui, X. Q.; Xu, Y. C.; Shang, B.; Zhang, Q. H.; Gu, L.; Fan, X. F.; Zheng, L. R.; Hou, C. M.; Huang, H. H. et al. Iridium-triggered phase transition of $MoS_2$ nanosheets boosts overall water splitting in alkaline media. *ACS Energy Lett.* **2019**, *4*, 368–374.

[144] Wang, C. Z.; Shao, X. D.; Pan, J.; Hu, J. G.; Xu, X. Y. Redox bifunctional activities with optical gain of $Ni_3S_2$ nanosheets edged with $MoS_2$ for overall water splitting. *Appl. Catal. B:Environ.* **2020**, *268*, 118435.

[145] Hou, J. G.; Zhang, B.; Li, Z. W.; Cao, S. Y.; Sun, Y. Q.; Wu, Y. Z.; Gao, Z. M.; Sun, L. C. Vertically aligned oxygenated-$CoS_2$-$MoS_2$ heteronanosheet architecture from polyoxometalate for efficient and stable overall water splitting. *ACS Catal.* **2018**, *8*, 4612–4621.